

# Analysis of the top-quark charged-current coupling at the LHeC

I. A. Sarmiento-Alvarado, Antonio O. Bouzas and F. Larios\*

*Departamento de Física Aplicada, CINVESTAV-Mérida,  
A.P. 73, 97310 Mérida, Yucatán, México*

In the context of  $SU(2)_L \times U(1)$  dimension six operators we study the potential of the LHeC to provide information on top quark effective interactions. We focus on single antitop production and how it is affected not only by the effective  $tbW$  coupling but also by four-fermion operators. Compared to the LHC, the LHeC provides a cleaner environment to make a precise measurement of the top quark production cross section. Therefore, this machine would give a much better assesment of  $V_{tb}$  in the context of the SM or  $V_L$  in the context of higher dimension operators. The LHeC could also give a slightly better measurement for  $V_R$ . For  $g_R$  the HL-LHC precise measurements of  $F_L$  and  $F_R$  (the  $W$ -boson helicity decay ratios of top) would yield better constraints than those obtained by the LHeC. Lepton-quark contact interactions would also be significantly better probed by the LHeC, since the only way of measuring them at the LHC would be through leptonic top decay which is hardly sensitive to these interactions.

PACS numbers: 14.65.Ha, 12.15.-y

## I. INTRODUCTION

The Large Hadron Electron Collider (LHeC) is the proposal of a new electron beam with an energy  $E_e = 60$  GeV or higher, to collide with one of the 7 TeV LHC proton beams. The expected luminosity of the LHeC could reach  $100 \text{ fb}^{-1}$  as the machine would run simultaneously with the high luminosity phase of the LHC (HL-LHC) that is expected to achieve a luminosity of  $3000 \text{ fb}^{-1}$  [1, 2]. Such a facility would be very useful in understanding, among other issues, parton and gluon interactions at very low  $x$  and very high  $Q^2$ , thus providing much needed complementary information for the physics program of the LHC. It could also be used to discover new resonances such as leptoquarks [3] and heavy Majorana neutrinos [4]. Moreover, compared to the LHC the LHeC gives us a much cleaner environment that could furnish very accurate information on Higgs physics [5, 6] and trilinear gauge boson couplings [7]. The proposed detector of the LHeC will have to meet special requirements such as [1]: 1) being able to detect a backward scattered electron

---

\* larios@mda.cinvestav.mx, corresponding author.

at angles up to 179 deg and a forward scattered final state at 1 deg; 2) optimum scale calibration for the measurement of  $\alpha_s$ ; 3) high resolution for the reconstruction of multi-jet final states; 4) good electron-hadron separation as required for electron identification at high rapidity; 5) hermetic calorimetry as required for a precise determination of  $\cancel{E}_T$  in charged current processes (single top production). We believe that these requirements will enable the LHeC to measure single top production, on the one hand with a precision in the few percent range for the leptonic mode, and on the other hand with a somewhat lower precision in the hadronic mode. This latter mode has not been measured in either the Tevatron or the LHC due to the enormous multi-jet activity. Therefore, the LHeC could provide a unique window in this case.

In this work we focus on single top quark production at the LHeC and on finding out how much information we can obtain on the dimension six  $SU(2)_L \times U(1)$  gauge-invariant operators that involve the top quark. Excluding flavor changing and CP violating effects, there are 31 independent operators. The LHC by itself will not be able to probe the effects of all these interactions. The input from future colliders like the LHeC and the ILC would be essential in making a complete analysis of the top quark.

Whenever a study of single top production as a probe of effective top-quark interactions is made, the framework of choice is the set of four independent on-shell  $tbW$  couplings with the structures  $\gamma_\mu P_{L,R}$  and  $\sigma_{\mu\nu} q^\nu P_{L,R}$ . However, it has been pointed out the importance of including the effects of the off-shell  $W$  to work out a truly complete description [8]. Those effects may be taken into account by means of an appropriate set of four-fermion operators, which should therefore be included in a complete study of single top production. In this paper we adopt this more general framework and base our analysis on the full basis of  $SU(2)_L \times U(1)$  operators including the relevant four-fermion ones.

Before discussing the LHeC sensitivity to the effective couplings we address the question of how well will this machine perform in comparison with the HL-LHC, with which it will run concurrently. We do this by means of a simplified evaluation of the limits on the couplings obtained from  $W$ -boson helicity fractions in top decays at the LHC, and from single top production at both the LHC and the LHeC.

In our study of the LHeC sensitivity to the effective couplings in single top production we obtain bounds on those couplings from global observables (as opposed to differential ones) such as the cross section and several kinematical asymmetries, computed at leading order (LO) at the partonic level. The experimental errors we assume are based on a detailed study of the Standard Model (SM) backgrounds. All of our computations and estimates are carried out at three electron-

beam energies  $E_e = 60$  and  $140$  GeV, which are typical proposed operational energies [1], and the higher  $E_e = 300$  GeV. This allows us to ascertain the energy dependence and the stability of our results. Another parameter we take into account is beam polarization, on which the sensitivity of observables to effective interactions involving right-handed electrons depends strongly.

In a previous report of single antitop production at the LHeC constraints were obtained for the four on-shell  $tbW$  couplings at a fixed  $E_e = 60$  GeV, and based on a set of four kinematical distributions for the leptonic channel and six for the hadronic channel [9]. Our work is an extension of that report in several ways: (1) we adopt the general framework of gauge invariant operators, that include the four  $tbW$  couplings plus four lepton-quark contact interactions, (2) we consider three values of  $E_e = 60, 140$  and  $300$  GeV, and (3) we obtain bounds based on the cross section as well as six kinematic observables for the leptonic channel and twenty-two for the hadronic channel (not all improve the bounds from the cross section, we show results only for those that do).

The paper is organized as follows. In section II we list the dimension six operators that are relevant for single antitop production at the LHeC. Since the LHeC will run along with the HL-LHC, in Section III we present an estimate of the sensitivity to the top-quark effective couplings of the LHeC as compared to the HL-LHC. In section IV we make a systematic study of the SM signal and background processes in antitop production and decay at the LHeC, discuss the appropriate cuts and their efficiency for background suppression, and estimate the experimental errors expected in the leptonic and hadronic channels. In section V we present the bounds we obtain on the anomalous couplings. We discuss bounds obtained from the cross section, and make an extensive survey of asymmetries of different kinematical observables to find the most sensitive among them. In this section we also discuss in detail the impact of electron-beam energy and polarization. Finally, in section VI we present our conclusions.

## II. TOP QUARK DIMENSION SIX OPERATORS

The discovery of the Higgs boson at the LHC, although still to be thoroughly tested in the future, suggests that the SM is indeed the correct model that explains all collider experiments up to the electroweak scale. However, the SM may be seen as an effective theory that is valid below a certain scale  $\Lambda$  [10]. At and above this scale the heavy degrees of freedom of a larger theory become apparent. Therefore, new physics effects may be properly described by an effective Lagrangian of

the form:

$$\mathcal{L} = \mathcal{L}_{\text{SM}} + \frac{1}{\Lambda^2} \sum_k \left( C_k O_k^{(6)} + \text{h.c.} \right) + \dots ,$$

where the ellipsis stands for operators of dimension higher than six. Many years ago a long list of gauge invariant dimension-six operators was introduced in Ref. [11]. Some time afterwards it became apparent that some of the operators involving the top quark were in fact redundant [12]. In particular, from the original list of 14 top-gauge boson operators it has been shown that only 8 are truly independent [13]. A revised general list of all the operators including those without the top quark, appears in Ref. [14]. It has been pointed out that this list in particular satisfies a so-called criterion of Potential-Tree-Generated operators, so that they may have the largest possible coefficients [15]. The complete list of dimension six operators for the top quark can be divided into three classes: (1) Operators that involve gauge bosons [13], (2) Operators that involve the Higgs but no gauge bosons [16], and (3) Four-fermion contact-interaction operators [17]. There are eight of the first type, one of the second type and 22 quartic operators. However, when the different flavor combinations as well as the CP even and odd parts are considered we end up with many independent variations of these operators. In the context of the single top production process  $ep \rightarrow \nu \bar{t}$  at the LHeC, however, we have only four gauge boson-top quark and four lepton-quark operators that are relevant. The description of new physics effects in single antitop quark production at the LHeC will thus be described by an effective Lagrangian of the form  $\mathcal{L}_{\text{eff}} = \mathcal{L}_{\text{SM}} + \mathcal{L}_{4f} + \mathcal{L}_{tbW}$ . We discuss in detail the Lagrangians  $\mathcal{L}_{4f}$  and  $\mathcal{L}_{tbW}$  below.

### A. Effective four fermion couplings of the top quark

Operators for four-fermion vertices have been analyzed in full generality in [17] in the context of the effective  $SU(2)_L \times U(1)$  gauge-invariant Lagrangian. Furthermore, a recent study on quark-quark operators in single top production at the LHC has been carried out in [18, 19]. Apart from flavor assignments, a complete list of 25 independent operators is given in Eqs. (2)-(5) of [17]. In this list, 3 operators are for lepton-lepton, 10 are for lepton-quark and 12 are for quark-quark interactions. As expected, if we take into account the different flavor combinations, we can find hundreds of variations. For the LHeC single-top process we are interested in flavor-diagonal lepton-quark operators involving the top quark and the first family of leptons, which selects only eight operators out of the 25 listed in [17]. They are shown in Table I, where  $q_{Li}$  and  $\ell_{Li}$  are the left-handed quark and lepton doublets, and  $e_{R1}$ ,  $u_{Rj}$ ,  $d_{Rj}$  are the right-handed electron and up

Charged Current	Neutral Current
$\mathcal{O}_{\ell q'}^{1331} = \bar{\ell}_{L1}\gamma^\mu q_{L3} \bar{q}_{L3}\gamma_\mu \ell_{L1}$	$\mathcal{O}_{\ell q}^{1133} = \bar{\ell}_{L1}\gamma^\mu \ell_{L1} \bar{q}_{L3}\gamma_\mu q_{L3}$
$\mathcal{O}_{qde}^{1133} = \bar{\ell}_{L1}e_{R1} \bar{d}_{R3}q_{L3}$	$\mathcal{O}_{\ell u}^{1331} = \bar{\ell}_{L1}u_{R3} \bar{u}_{R3}\ell_{L1}$
$\mathcal{O}_{q\ell e}^{3113} = \bar{q}_{L3}e_{R1} (\bar{\ell}_{L1}\epsilon)^T u_{R3}$	$\mathcal{O}_{qe}^{1331} = \bar{q}_{L3}e_{R1} \bar{e}_{R1}q_{L3}$
$\mathcal{O}_{\ell q e}^{1133} = \bar{\ell}_{L1}e_{R1} (\bar{q}_{L3}\epsilon)^T u_{R3}$	$\mathcal{O}_{eu}^{1133} = \bar{e}_{R1}\gamma^\mu e_{R1} \bar{u}_{R3}\gamma_\mu u_{R3}$

TABLE I: Flavor diagonal quartic Lepton-Quark operators that involve top quarks and electrons. The ones on the left column contribute to single top production at the LHeC.

and down quark singlets.

The operators on the left column of Table I are of CC type, therefore relevant to the LHeC, whereas those on the right column are of NC type, relevant for  $t\bar{t}$  production at a  $e^+e^-$  collider like the ILC [17]. The CC operator  $\mathcal{O}_{\ell q'}^{1331}$ , which contains terms of the form  $\bar{\nu}_L\gamma^\mu e_L \bar{b}_L\gamma_\mu t_L$ , is of special interest as it is the only one that can lead to an interference term with the SM amplitude. It can be generated by a heavy  $W'$  or a vector leptoquark [20, 21]. The other three operators, that involve a right-handed electron can be generated by a heavy charged Higgs or a scalar leptoquark [22]. The four-fermion Lagrangian defined by the CC type operators in Table I is then:

$$\begin{aligned} \Lambda^2 \mathcal{L}_{4f} &= C_1 \mathcal{O}_{\ell q'}^{1331} + [C_2 \mathcal{O}_{qde}^{1133} + C_3 \mathcal{O}_{q\ell e}^{3113} + C_4 \mathcal{O}_{\ell q e}^{1133} + h.c.] \\ &= C_1 (\bar{\nu}_L\gamma^\mu t_L \bar{b}_L\gamma_\mu e_L + h.c.) + [C_2 \bar{\nu}_L e_R \bar{b}_R t_L + C_3 \bar{b}_L e_R \bar{\nu}_L t_R + C_4 \bar{\nu}_L e_R \bar{b}_L t_R + h.c.], \end{aligned} \quad (1)$$

where  $\mathcal{O}_{\ell q'}^{1331}$  is already Hermitian, but the other three operators are not. The coefficient  $C_1$  must therefore be real, and  $C_{2,3,4}$  are complex, their imaginary parts giving rise to CP-odd interactions.

## B. Effective $tbW$ couplings of the top quark

The complete list of top-gauge boson operators is given in Eqs. (3) and (4) of [13]. Notice that not all of the operators in that list are independent. The operators that modify the CC effective  $tbW$  coupling are:

$$\begin{aligned} \mathcal{O}_{\phi q}^{(3,ij)} &= \frac{i}{2} \phi^\dagger \tau^I D_\mu \phi \bar{q}_{Li} \gamma^\mu \tau^I q_{Lj}, & \mathcal{O}_{\phi\phi}^{ij} &= i \tilde{\phi}^\dagger D_\mu \phi \bar{u}_{Ri} \gamma^\mu d_{Rj}, \\ \mathcal{O}_{uW}^{ij} &= \bar{q}_{Li} \sigma^{\mu\nu} \tau^I u_{Rj} \tilde{\phi} W_{\mu\nu}^I, & \mathcal{O}_{dW}^{ij} &= \bar{q}_{Li} \sigma^{\mu\nu} \tau^I d_{Rj} \phi W_{\mu\nu}^I. \end{aligned} \quad (2)$$

We use standard notation with  $I, J, K$   $SU(2)$  gauge indices,  $\tau^I$  Pauli matrices, and  $\phi$  the SM Higgs doublet with  $\tilde{\phi} = i\tau^2 \phi^*$  [13]. For every operator in (2) there are 3 or more variations depending on the flavor content. Throughout this paper we consider only flavor-diagonal interactions,

corresponding to flavor indices  $ij = 33$  in (2). The flavor-changing (FC) combinations 13 and 23 do contribute to single-top production but we will not consider them. The operator  $O_{\phi q}^{(3,33)}$  is Hermitian, and the other three flavor-diagonal operators can be decomposed into Hermitian and anti-Hermitian parts. In Table I of [23] the CP-even and CP-odd parts of these operators are displayed in detail. In Table II of [23] the constraints from electroweak data and  $b \rightarrow s\gamma$  observables can be found. Those constraints were found by taking into account only one operator at a time, but in general there are correlations among coefficients [24–26].

We write the effective  $tbW$  Lagrangian as:

$$\Lambda^2 \mathcal{L}_{tbW} = C_{\phi q} O_{\phi q}^{(3,33)} + [C_{\phi\phi} O_{\phi\phi}^{33} + C_{tw} O_{uW}^{33} + C_{bW} O_{dW}^{33} + h.c.], \quad (3)$$

where  $C_{\phi q}$  is real and  $C_{\phi\phi}$ ,  $C_{tw}$ ,  $C_{bW}$  are complex, their imaginary parts multiplying the anti-Hermitian parts of the corresponding operators in (3) and giving rise to CP-odd interactions. A recent phenomenological study on the imaginary parts of the effective  $tbW$  couplings at the LHC is given in [27].

We have not included in (3) the operator  $O_{qW}^{ij} = \bar{q}_{Li} \gamma^\mu \tau^I D^\nu q_{Lj} W_\mu^I$ , that is independent of the set of operators (2) and gives an important contribution to the single-top production process. In fact, as pointed out in [8], a complete parametrization of new physics effects from the trilinear  $tbW$  coupling should involve the contribution from this operator. However,  $O_{qW}^{ij}$  can be written as a linear combination of the operators (2) and the four-fermion operators of CC type in Table I. We can use the equation of motion for the  $W$  field [8]:

$$(D^\nu W_{\nu\mu})^I = \frac{g}{2} \sum_{k=1}^3 (\bar{q}_{Lk} \gamma_\mu \tau^I q_{Lk} + \bar{\ell}_{Lk} \gamma_\mu \tau^I \ell_{Lk}) + i\frac{g}{2} [\phi^\dagger \tau^I D_\mu \phi - (D_\mu \phi)^\dagger \tau^I \phi],$$

to apply it in the expression  $O_{qW}^{ij} + (O_{qW}^{ji})^\dagger = (\bar{q}_{Li} \gamma^\mu \tau^I q_{Lj}) (D^\nu W_{\nu\mu})^I$ . Then, by means of a Fierz rearrangement of the field operators, we can write  $\bar{q}_{Li} \gamma^\mu \tau^I q_{Lj} \bar{\ell}_{Lk} \gamma_\mu \tau^I \ell_{Lk} = 2O_{\ell q'}^{kjik} - O_{\ell q}^{kkij}$ , where the operators  $O_{\ell q'}^{ijkl}$  and  $O_{qq'}^{ijkl}$  are four-fermion lepton-quark and quark-quark contact interactions [17]. Therefore:

$$\begin{aligned} O_{qW}^{ij} + (O_{qW}^{ji})^\dagger &= \frac{g}{2} \left( O_{\phi q}^{(3,ij)} + (O_{\phi q}^{(3,ji)})^\dagger \right) \\ &+ g \sum_{k=1}^3 \left( O_{\ell q'}^{kjik} - \frac{1}{2} O_{\ell q}^{kkij} \right) + 2g \sum_{k=1}^3 \left( O_{qq'}^{kjik} - \frac{1}{2} O_{qq}^{kkij} \right), \end{aligned} \quad (4)$$

which in the case of single-top production at the LHeC of interest to us reduces to  $O_{qW}^{33} + (O_{qW}^{33})^\dagger = gO_{\phi q}^{(3,33)} + gO_{\ell q'}^{1331} + \dots$ . We take advantage of this relation and choose to perform our study with

the quartic terms instead of  $O_{qW}^{ij}$ . Notice that these terms can enter in both the top decay and production process.

As is common practice in the literature, we can write down the effective  $tbW$  couplings in terms of form factors. Let us separate those terms in  $\mathcal{L}_{tbW}$  that generate the effective  $tbW$  vertex [8, 13]:

$$\mathcal{L}_{tbW} = -\frac{g}{\sqrt{2}}\bar{b}\left(\gamma^\mu(V_L P_L + V_R P_R) - \frac{i\sigma^{\mu\nu}q_\nu}{m_W}(g_L P_L + g_R P_R)\right)tW_\mu^- + h.c. \quad (5)$$

Notice that  $V_{L(R)} \equiv F_1^{L(R)}$  and  $g_{L(R)} \equiv -F_2^{R(L)}$  as in Ref. [23]. The relation between the form factors and the operator coefficients in (3) is given by:

$$V_L = V_{tb} + \frac{1}{2}\frac{v^2}{\Lambda^2}C_{\phi q}, \quad V_R = \frac{1}{2}\frac{v^2}{\Lambda^2}C_{\phi\phi}, \quad g_R = \sqrt{2}\frac{v^2}{\Lambda^2}C_{tW}, \quad g_L = \sqrt{2}\frac{v^2}{\Lambda^2}C_{bW}. \quad (6)$$

For concreteness we set  $\Lambda \equiv 1$  TeV, and write the dimensionful parameters in the operators in units of TeV, namely,  $v = 0.246$ ,  $m_t = 0.173$  and  $m_W = 0.08$ . We can go back to a general  $\Lambda$  by just replacing the anomalous coupling constants  $C$  by  $C/\Lambda^2$ .

### III. TOP QUARK DECAY AND SINGLE TOP PRODUCTION

The LHeC will run along with the high luminosity phase of the LHC, so that by the time the LHeC experiment delivers useful data so will the other experiments at the LHC. Precision measurements of  $t\bar{t}$  production, top decay, LHC and LHeC single-top production, and more, will be analysed simultaneously. In this section we present a broad-brush picture of what to expect from the LHeC as compared to the performance of the LHC by the time the data from the very high luminosity phase becomes available. For that purpose, we use three independent observables relevant to the study of the  $tbW$  and top quark quartic couplings, namely, the  $W$ -boson helicity fractions, the LHC and the LHeC single-top production cross sections. Below, we proceed in two steps. First, we compute the observables in the approximation of two-body final states, in order to estimate the bounds on the anomalous couplings from recent measurements by CMS of  $W$  helicity fractions in top decays, and of single top production [28–30]. Measurements on single top production by the ATLAS collaboration are also available but with a larger error [31]; for instance, at  $\sqrt{s} = 8$  TeV ATLAS measures  $\sigma^{t\text{-}chan}(t + \bar{t}) = 82.6$  with 14.2% error, whereas CMS measures  $\sigma^{t\text{-}chan}(t + \bar{t}) = 83.6$  with 9.3%. We will only use the CMS results, which provide with the most constraining bounds. We also compare our results with more precise analyses done in the literature to test whether our formulas yield good approximations. Finally, we apply this same approach to make a conservative estimate of what the bounds will be like once the data from the HL-LHC and

the LHeC are available. In the remainder of this section we take the anomalous couplings to be real for simplicity. We should bear in mind that the estimated bounds for the LHeC and the HL-LHC in this section are only conservative approximations. We expect both machines to actually yield better constraints based on all the by then available data and on more powerful techniques of data analysis.

### A. The polarized $t \rightarrow bW$ decay ratios $F_0$ , $F_L$ and $F_R$

It is well known that the helicity of the  $W$  boson in the  $t \rightarrow bW$  decay can be used to study the effective  $tbW$  coupling [32, 33]. The CMS collaboration has published precise measurements of the decay ratios and have used their results to set bounds on the effective  $g_L$  and  $g_R$  parameters in (5) [28]. Another recent study based on CMS measurements can be found in [34]. In our study, we would like to use a simplified set of formulas to help us make a conservative estimate of the possible bounds that the future HL-LHC could achieve and compare them with the estimated bounds from the LHeC experiment.

The tree level decay  $t \rightarrow bW$  with the general  $tbW$  vertex has been analyzed in [32, 33]. At second order in the anomalous couplings, the longitudinal, left-handed and right-handed  $W$  polarization fractions are:

$$\begin{aligned} F_0 &= F_0^{\text{SM}} - 0.926g_L^2 + 0.709g_R + 0.457g_R^2 + 0.709g_L V_R - 0.709g_R \delta V_L, \\ F_L &= F_L^{\text{SM}} - 0.468g_L^2 - 0.709g_R - 0.457g_R^2 + 0.591g_L V_R - 0.303V_R^2 + 0.709g_R \delta V_L, \\ F_R &= F_R^{\text{SM}} + 1.394g_L^2 - 1.300g_L V_R + 0.303V_R^2, \end{aligned} \quad (7)$$

where we have set  $m_t = 172.5$  GeV and  $m_t/m_W = 2.145$ , and we have neglected terms proportional to  $m_b$ . In this approximation the SM helicity fractions are  $F_0^{\text{SM}} = 0.697$ ,  $F_L^{\text{SM}} = 0.303$  and  $F_R^{\text{SM}} = 0$ . At higher order and with  $m_b$  terms there is a small but non-zero fraction  $F_R = 0.0017$ , and a slight 2.6% increase in the  $F_L$  value as shown in Table II. In the limit where  $V_R = g_R = g_L = 0$ , the expressions in (7) are independent of  $V_L$ . Hence, these quantities can not be used to probe that coupling (or the CKM  $V_{tb}$  coefficient). It is also apparent from (7) that  $F_L$  is mostly sensitive to  $g_R$ , and  $F_R$  is mostly sensitive to  $g_L$  and  $V_R$ .

In principle, there are also contributions to the top quark width coming from the quartic operators that we are considering here. However, they are about two orders of magnitude lower than the contribution from the  $tbW$  coefficients [35]. In this work we do not include the negligible effects of four-fermion operators on top decay.



Below, we will show the bounds obtained using the latest (published) measurement by CMS on  $F_L$  and  $F_R$  [28]. In doing so, we will use for  $F_{0,L,R}^{\text{SM}}$  in (7) the SM values with full QCD corrections and  $m_b$  terms as shown in Table II. The experimental data on the branching ratios  $F_{0,L,R}$  are from last year CMS publication [28]. The errors presented there are evenly distributed in statistical and systematic origins. For the purpose of making an estimate of a future measurement in the HL-LHC era we will assume that the errors then will be of mainly systematic origin and about half the size of current results (see Table III).

Notice that there is a recent CMS internal report with new results (and with lower errors) [36]. These values have already been used in the literature [27, 34, 37]. We have not used these results in our estimate for the following reason: their value of  $F_L$  is  $0.35 \pm 0.01 \pm 0.024$  and it is already more than  $1\sigma$  above the SM prediction. Therefore, the allowed region for  $g_L$  when  $g_R \simeq 0$  is dramatically reduced as compared to the region allowed by the previous year's data in [28]. See Table I in [34]. It is likely that future studies will shift the  $F_L$  ratio back to the SM prediction, and then the allowed region will look more like the one obtained with the latest published report [28].

## B. Single top quark production

Below we will discuss the constraints on the effective couplings that come from  $\sigma^{t+s}$  the inclusive  $t$ -channel plus  $s$ -channel production of single top at the Tevatron [38]. Also, we will use the inclusive  $\sigma^t$   $t$ -channel production measured by CMS with both  $\sqrt{s} = 7$  and 8 TeV [29, 30]. From these measurements, the CMS collaboration obtains a 68% confidence level (CL)+ value for the SM  $tbW$  coupling [30]:  $|V_{tb}| = 0.998 \pm 0.038(\text{exp.}) \pm 0.016(\text{theo.})$ . This is consistent with the value  $V_L = 0.994 \pm 0.046$  obtained with our simplified method. In addition, we will make an estimate from a similar measurement at the future HL-LHC with  $\sqrt{s} = 14$  TeV. The SM values as well as the most recent experimental measurements we use for our analysis are given in Table II.

We can write down the single top production cross section at hadron colliders in terms of the effective couplings. Since the  $tbW$  vertex occurs in the production and decay vertices, we expect a polynomial of fourth degree. However, in this simplified analysis we will take the top decay exactly as in the SM with  $V_L = 1$ . Therefore, the expression for the cross section contains only linear and square terms. We find it convenient to define the ratio  $R_\sigma$  as follows:

$$R_\sigma \equiv \frac{\sigma_{V_L}^{\text{SM}} + \Delta\sigma}{\sigma_{V_L=1}^{\text{SM}}} = V_L^2 + a_{12}g_R + a_{22}g_R^2 + a_{33}V_R^2 + a_{44}g_L^2 + a_{15}g_\times + a_{55}g_\times^2, \quad (8)$$

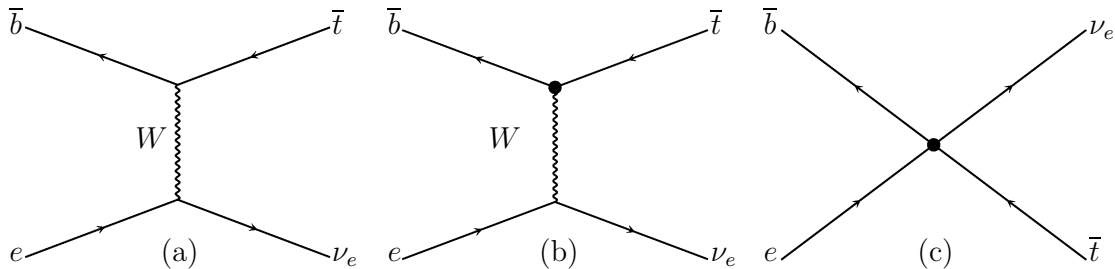


FIG. 1: Feynman diagrams for single-top production in  $e^-p$  collisions. The top decay process is assumed to occur as in the SM.

	$\sigma^{t+s}(t+\bar{t})$	$\sigma^t(t+\bar{t})$	$\sigma^t(t+\bar{t})$	$F_L$	$F_R$
	Tevatron	LHC7	LHC8	CMS	CMS
Theory	3.38	65.9	87.2	0.311	0.0017
Experiment	$3.04 \pm 0.57$	$67.2 \pm 6.1$	$83.6 \pm 7.8$	$0.310 \pm 0.031$	$0.008 \pm 0.018$

TABLE II: Theoretical values and experimental measurements of cross sections in units of pb and decay ratios used in this study. References for the Tevatron  $\sigma^{t+s}(t+\bar{t})$ , the LHC  $\sigma^t(t+\bar{t})$  and the top decay  $W$ -boson helicity ratios  $F_L$  and  $F_R$  are [39–41] (theory) and [28, 30, 38] (experiment).

where by  $\sigma^{\text{SM}}$  we mean the SM prediction with  $V_L$  not necessarily equal to one. The coupling constant  $g_\times$  in (8) plays a role analogous to  $C_1$  for four-quark interactions,  $g_\times/\Lambda^2$  being the coefficient of the operator  $O_{qq}^{1331} = \bar{b}_L \gamma^\mu t_L \bar{u}_L \gamma_\mu d_L$  in the effective Lagrangian. It was introduced in Ref. [8], where the contribution of  $O_{qq}^{1331}$  was considered along with the effective  $tbW$  vertex. For the sake of simplicity we are considering interference terms with the SM amplitude ( $V_L = 1$ ) but we are disregarding interference terms between the anomalous couplings (such as terms proportional to  $V_R g_L$ ). There are no linear terms for  $V_R$  and  $g_L$  because their interference with the SM is suppressed by  $m_b$ . In this section we will only consider terms that are the most significant.

We will also define the ratio  $R_\sigma$  for single top production at the LHeC as shown in Fig. 1. In this case we include the contribution from the four lepton-quark operators of Eq. (1):

$$R_\sigma = V_L^2 + b_{12}g_R + b_2g_R^2 + b_3V_R^2 + b_4g_L^2 + b_{15}C_1 + b_5C_1^2 + b_6C_2^2 + b_7C_3^2 + b_8C_4^2, \quad (9)$$

where we have, as before, ignored the effects from top decay. Eventually, in Eq. (17) below we will write again this cross section ratio in a general context. There, effects from the decay of top will be included. In addition, the effective couplings which so far have been considered real will be taken as complex.

The numerical values for the coefficients in (8) and (9), given in Appendix A, have been obtained

	HL-LHC $F_L$	HL-LHC $F_R$	HL-LHC $\sigma^t(t+\bar{t})$	LHeC60
Theory	0.311	0.0017	248.0	1.73
Exp. Error	$\pm 0.016$	$\pm 0.010$	$\pm 7\%$	$\pm 4\%$

TABLE III: Assumed future experimental errors and associated SM values for  $W$ -boson helicity ratios of top decay and single top quark production cross sections in units of pb at the HL-LHC and the LHeC. The LHC (14 TeV) NNLO result is given in [40]. The value for the LHeC ( $E_e = 60$  GeV) is at LO.

at LO with the program CalcHEP [42]. For the inclusive production at the Tevatron we obtain  $\sigma^{t+s}(t+\bar{t}) = 2.5$  pb, and for the inclusive t-channel top production at the LHC at  $\sqrt{s} = 7, 8, 14$  TeV we obtain  $\sigma^t(t+\bar{t}) = 56.6, 74.8, 221.0$  pb. The values shown in Table II include QCD corrections that typically increase the cross sections by about 15%. These are the values we actually use for  $\sigma^{\text{SM}}$ , not the LO ones. We obtain bounds on the effective couplings by comparing  $\sigma^{\text{SM}}R_\sigma$  with the experimental values and  $1\sigma$  errors also given in Table II. In the case of the future LHC run at 14 TeV and the proposed LHeC we assume that the experimental central values will turn out to be exactly equal to the SM prediction. The bounds obtained will then be defined by just the assumed experimental errors, which are listed in Table III. For the case of the HL-LHC we assume that the total error will go from the current 9.4% to a 7%. For the case of the LHeC the 4% error is somewhat larger than the estimated minimum of 3% we will present in Section IV in a detailed study of the semileptonic channel of single-top production and decay.

### C. Current and future bounds

Bounds obtained for each coupling and with our procedure are shown in Table IV. They are based on  $1\sigma$  deviations with 68% CL. For the sake of comparing with other recent bounds in the literature we point out that at 95% CL our bounds from the current LHC data would be  $|\delta V_L| < 0.09$ ,  $|V_R| < 0.42$ ,  $|g_L| < 0.34$ , and  $g_R = 0.11 \pm 0.36$  which are consistent with the bounds obtained in [34] based on the same CMS data of Table II (see Figs. 2 and 4 in [34]). Let us discuss these bounds for each coupling below.

Concerning the quartic operator coefficients  $C_1$  and  $g_x$ . Comparing with the bounds on the  $tbW$  vertex these coefficients may look to be weakly bounded. However, this is a matter of normalization. In fact, if we compare with the coefficients of the  $tbW$  operators in Eqs. (3) and (6)  $C_{\phi q} = 33.0\delta V_L$ ,  $C_{\phi\phi} = 33.0V_R$ ,  $C_{tW} = 11.66g_R$  and  $C_{bW} = 11.66g_L$  we observe that the four fermion operators are better constrained. For instance, the LHC current bounds for  $tbW$  are  $|C_{\phi q}| < 1.5$ ,  $|C_{\phi\phi}| < 7.2$ ,

$|C_{bW}| < 2.1$  and  $C_{tW} = 1.3 \pm 2.8$ , whereas the bound on  $\bar{b}_L \gamma^\mu t_L \bar{u}_L \gamma_\mu d_L$  is  $g_\times = -0.14 \pm 0.95$ . Concerning the bounds on the coefficients  $C_k$  with  $k = 2, 3, 4$  that are not shown in Table IV. For the LHeC at  $E_e = 60$  GeV they are  $|C_k| < 4.5$  ( $k = 2, 4$ ) and  $|C_3| < 2.6$  which are rather weak compared with  $|C_1| < 0.34$ . The operators of  $C_k$  with  $k = 2, 3, 4$  in Eq. (1) are associated with a right-handed electron and there is no interference with the SM.

Concerning  $V_L$ . Since the decay ratios  $F_L$  and  $F_R$  change very little with  $V_L$  (or not at all if the other couplings are zero) we do not obtain bounds from them. This also applies to the four fermion operators. The Tevatron result is about 11% lower than the SM prediction with  $V_L = 1$ , so it is suggesting a lower value of 0.925. On the other hand, the LHC results for 7 and 8 TeV balance each other. One is 2% above the theoretical values and the other is 4% below. Their combined effect suggests  $V_L = 0.994 \pm 0.046$  which is rather close to 1. Notice that the allowed region we obtain is somewhat weaker but still consistent with the more precise value of  $0.998 \pm 0.038$  obtained by CMS [30] (68% CL). For the LHC14 we assume that experimental and theoretical values coincide within an error of 7%. This directly translates to  $V_L = 1 \pm 0.036$ . The lesson we learn here is that according to this estimate the HL-LHC will not make a major improvement on  $V_L$ . In this scenario, if the LHeC reaches the 4% error that we assume, it will indeed yield a much better measurement of  $V_L$ . On the other hand, when we take into account the effects from the 4-fermion operators the constraints on  $V_L$  tend to relax. This, of course also happens with the LHC single top production [8]. However, at the LHC there are two independent channels of single top production ( $s$ -channel and  $t$ -channel) that are sensitive to the 4-fermion interaction. This means that the combination of both measurements ends up constraining again the allowed region of  $V_L$  that is otherwise poorly constrained by the  $t$ -channel measurement alone [8, 34]. Currently, the measurement of the  $s$ -channel cross section at the LHC has proven to be very challenging [31, 43], and no bounding regions can be obtained from this mode. At the LHeC there is no  $s$ -channel mode, and we have to rely on the  $t$ -channel only to disentangle the effects of both interactions.

Concerning  $g_R$  that involves the left chirality of the bottom quark, there is significant interference with the SM amplitude. As shown in the tables in Appendix A this is always a negative interference, therefore there is more allowed space for positive values of  $g_R$ . The LHC yields stronger constraints (via single top production) than the LHeC because the vertex proportional to  $g_R$  depends on energy, which is larger at the LHC. However, the bounds obtained from the single top measurement are about one order of magnitude lower than the bounds coming from the decay ratio  $F_L$  whose measurement will be based on the much larger sample of  $t\bar{t}$  events. Concerning  $g_L$ , again the decay ratio  $F_R$  is more likely to be a better probe than the LHeC although not with a

	$V_L$	$V_R$	$g_R$	$g_L$	$g_{\times}; C_1$
$F_L$	–	$\pm 0.34$	$\pm 0.044$	$\pm 0.28$	–
$F_R$	–	$\pm 0.30$	–	$\pm 0.14$	–
Tevatron	$0.925 \pm 0.13$	$\pm 0.32$	$0.25 \pm 0.30$	$\pm 0.17$	$0.68 \pm 1.22$
LHC	$0.994 \pm 0.046$	$\pm 0.22$	$0.11 \pm 0.24$	$\pm 0.18$	$-0.14 \pm 0.95$
$F_L$	–	$\pm 0.23$	$\pm 0.022$	$\pm 0.19$	–
$F_R$	–	$\pm 0.18$	–	$\pm 0.09$	–
LHC14	$1 \pm 0.036$	$\pm 0.27$	$0.09 \pm 0.22$	$\pm 0.21$	$\pm 0.53$
LHeC	$1 \pm 0.02$	$\pm 0.17$	$0.19 \pm 0.29$	$\pm 0.13$	$\pm 0.34$

TABLE IV: Bounds on couplings (68% CL). The upper half is from recent experimental results. The lower half is an estimate of the future results of the HL-LHC and LHeC.

big difference.

Notice that the LHC14 bounds on  $V_R$  and  $g_L$  are actually weaker than the current bounds based on the LHC run at 8 TeV. What happens is that for these (right handed bottom) couplings there is no interference with the SM amplitude in the zero  $m_b$  limit. The contribution to single top production can only be positive and proportional to the square of the couplings. Since the theoretical prediction is already above the experimental value, there is little allowed region left for  $V_R$  and  $g_L$ . If, as we have assumed here, the 14 TeV run yields a measurement that is equal to the SM prediction, the allowed region will actually be increased. This is so even if the experiment achieves a lower experimental error. On the other hand, even though the ratio  $F_R$  could yield a tight bound on  $V_R$ , the LHeC we estimate could achieve a similar constraint.

The results of the simplified analysis carried out in this section, collected in Table IV, provide a semi-quantitative picture of the most likely scenarios as to how much the LHeC could improve the couplings analyses performed at the HL-LHC. It appears that the LHeC would give better constraints than the HL-LHC on  $V_L$ ; competitive and possibly better constraints on  $V_R$ ; weaker, but comparable bounds on  $g_L$  and poorer constraints on  $g_R$ . As for contact interactions, the two machines will probe different sets: quark-quark operators at the LHC and lepton-quark operators at the LHeC. We expect this semi-quantitative picture, obtained here by means of a simplified calculational approach, to remain valid in the context of a technically more detailed analysis as given in Section V below.

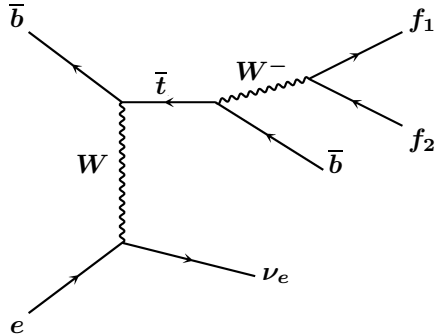


FIG. 2: Feynman diagram for single-top production and decay in  $e^-p$  collisions.

#### IV. SINGLE-TOP PRODUCTION AT THE LHEC IN THE STANDARD MODEL

The scattering amplitude for single-antitop production in  $e^-p$  collisions in the SM, followed by antitop decay, is given by the Feynman diagram in Figure 2. Throughout this paper we restrict ourselves to light charged leptons in the final state, which we take to be massless. Thus, in the antitop-decay leptonic channel the final-state fermions in the figure are  $f_1, f_2 = e^-, \bar{\nu}_e$  or  $\mu^-, \bar{\nu}_\mu$ . In the hadronic channel  $f_1, f_2 = d, \bar{u}$  or  $s, \bar{c}$ . We work with four massless flavors so, in particular, we neglect CKM mixing.

In the remainder of this section we discuss the cross sections for single-antitop production in  $e^-p$  collisions in the SM, in both the leptonic and hadronic channels. We analyze the signal process as well as its irreducible and reducible backgrounds, and estimate the statistical and systematical errors. Our statistical error estimates are based on the assumption that the LHeC will achieve a total integrated luminosity  $\mathcal{L} = 100 \text{ fb}^{-1}$ . In all cases we set  $m_t = 172.5 \text{ GeV}$ ,  $m_b = 4.7 \text{ GeV}$ ,  $m_Z = 91.1735 \text{ GeV}$ ,  $m_W = 80.401 \text{ GeV}$ ,  $m_h = 125 \text{ GeV}$ ,  $\alpha = 1/132.507$ ,  $G_F = 1.1664 \times 10^{-5} \text{ GeV}^{-2}$ ,  $\alpha_S(m_Z) = 0.118$ , and the Higgs vacuum-expectation value  $v = 246.2185 \text{ GeV}$ . The computation of the cross sections for the various different processes considered in this section were carried out with the matrix-element Monte Carlo simulation program MADGRAPH5\_AMC@NLO version 2.1.0 [44, 45] at tree level. Where needed, the events generated by the simulation were analyzed with MADANALYSIS5 version 1.1.9 [46]. We set the renormalization and factorization scales fixed at  $\mu_R = m_t = \mu_F$  and used the parton-distribution functions CTEQ6-L1 as implemented in MADGRAPH5.

An electron-proton collider such as the LHeC offers the opportunity of performing measurements with a polarized electron beam. Current accelerator technology makes it possible to achieve longitudinal polarization at the interaction points in electron storage rings, as was done at HERA where

polarizations of 65% were reached [47]. In linear accelerators, electron beam polarizations of up to 80% can be achieved reliably for long periods of time as was done at SLC [48]. For our purposes in this paper the most interesting case is that of right-handed electron polarization,  $0 \leq \mathcal{P}_e \leq +1$ , so that below we discuss the signal and backgrounds cross sections for electron polarizations  $\mathcal{P}_e = 0$ ,  $+0.4$  and  $+0.7$ .

### A. Standard Model: Leptonic channel

In the leptonic mode the signal ( $S$ ) and signal plus irreducible background ( $S + B$ ) in the SM are defined as

$$S : e^- p(\bar{b}) \rightarrow \bar{t} \nu_e \rightarrow \bar{b} \ell^- \bar{\nu}_\ell \nu_e, \quad S + B : e^- p(\bar{b}) \rightarrow \bar{b} \ell^- \bar{\nu} \nu, \quad (10)$$

where the final-state charged leptons are restricted to the light flavors  $\ell = e, \mu$ . In the SM the signal process  $S$  involves only two Feynman diagrams, corresponding to Figure 2 with  $f_1, f_2 = \ell^-, \bar{\nu}_\ell$ . The irreducible background  $B$  comprises 51 diagrams with four electroweak vertices, see Figure 3, out of which 20 have  $\ell^- \bar{\nu} \nu = e^- \bar{\nu}_e \nu_e$  in (10), 11 have  $\ell^- \bar{\nu} \nu = e^- \bar{\nu}_\mu \nu_\mu$ , 11 have  $e^- \bar{\nu}_\tau \nu_\tau$ , and 9 have  $\mu^- \bar{\nu}_\mu \nu_e$ . Furthermore, there are 33 diagrams of the type  $e^- \bar{b} \rightarrow e^- \bar{b} f f$  in which the fermion line beginning with the initial electron goes through NC vertices only, and 18 of the form  $e^- \bar{b} \rightarrow \nu_e \bar{b} f f$  in which one CC vertex is attached to that fermion line. For the computation of cross sections we apply phase-space cuts on the final-state momenta. We consider several sets of cuts defined as

$$\begin{aligned} L_1 : & \quad |\vec{p}_T(\ell)| > 20 \text{ GeV}, |\vec{p}_T(\bar{b})| > 20, \\ L_2 : & \quad L_1, \cancel{E}_T > 25 \text{ GeV}, \\ L_3 : & \quad L_2, |\eta(\ell)| < 2.5, |\eta(\bar{b})| < 2.5, \\ L_4 : & \quad L_3, \Delta R(\ell, \bar{b}) > 0.4, \end{aligned} \quad (11)$$

where  $\Delta R = \sqrt{(\Delta\eta)^2 + (\Delta\varphi)^2}$  is the distance in the  $\eta$ - $\varphi$  plane, in the laboratory frame. The cuts (11) are standard centrality and isolation cuts, needed to ensure a hard partonic scattering and to render the background processes free from infrared instabilities due to photon  $t$ -channel exchange. With cuts  $L_4$ , at the three electron energies considered here more than 95% of the irreducible background originates in the 12 diagrams from Figure 3 in which  $\ell^-, \bar{\nu}$  are the decay products of an on-shell  $W^-$ , as happens also in the signal process. Furthermore, we cannot impose cuts on the would-be  $\bar{t}$  decay products constraining them to the  $\bar{t}$  mass shell, as there are two

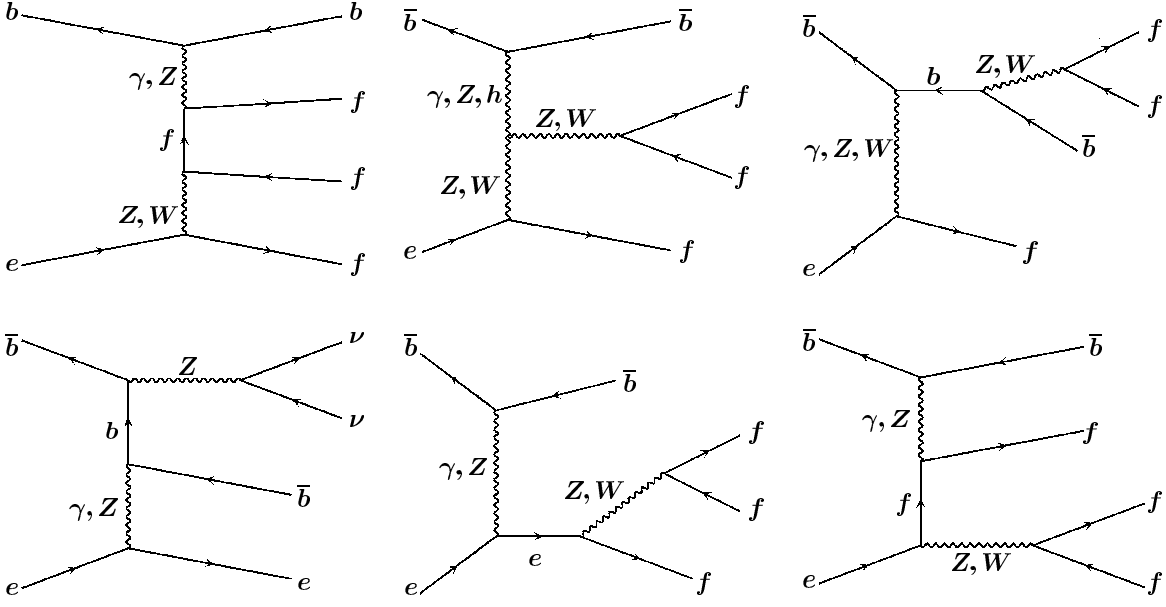


FIG. 3: Feynman diagram for the irreducible background to leptonic-channel single-top production.  $\nu$  refers to  $\nu_{e,\mu,\tau}$  and  $f$  to  $e^-$ ,  $\mu^-$  or  $\nu$ .

	$E_e = 60 \text{ GeV}$			$E_e = 140 \text{ GeV}$			$E_e = 300 \text{ GeV}$		
	$\sigma_S$	$\sigma_B$	$\sigma_{S+B}$	$\sigma_S$	$\sigma_B$	$\sigma_{S+B}$	$\sigma_S$	$\sigma_B$	$\sigma_{S+B}$
$\emptyset$	0.3701			1.1210			2.519		
$L_1$	0.2891	0.0028	0.2892	0.8754	0.0108	0.8688	1.967	0.0318	1.942
$L_2$	0.2482	0.0024	0.2477	0.7564	0.0095	0.7507	1.713	0.0289	1.693
$L_3$	0.2042	0.0018	0.2034	0.7022	0.0084	0.6971	1.647	0.0268	1.626
$L_4$	0.2030	0.0018	0.2028	0.6984	0.0084	0.6931	1.640	0.0268	1.618

TABLE V: Cross sections in pb for the signal  $S$ , irreducible background  $B$  and signal-plus-background  $S+B$  processes defined in (10), with the cuts (11).  $\emptyset$  refers to the cross sections without cuts.

neutrinos in the final state. Therefore, a small signal-background interference remains that turns out to be destructive. As a consequence, the ratios  $\sigma_B/\sigma_S$  and  $(\sigma_{S+B} - \sigma_S)/\sigma_S$  have different sign, and the former is larger than the absolute value of the latter. In what follows we make the more conservative choice of using the larger ratio  $\sigma_B/\sigma_S$  as a measure of the systematic error originating in the irreducible background. In Table V we summarize the effects of the cuts (11) on the SM signal and irreducible background.

The main source of reducible background to the signal process (10) is  $b$ -jet mistagging from the the flavor-diagonal processes

$$e^- p(c) \rightarrow c \ell^- \nu \bar{\nu}, \quad e^- p(q) \rightarrow q \ell^- \nu \bar{\nu}, \quad (12)$$



	$\sigma_c$ [pb]	$\sigma_q$ [pb]	$\delta_{\text{mis}}\sigma$ [pb]
60 GeV	0.006	0.080	0.0014
140 GeV	0.021	0.220	0.0043
300 GeV	0.055	0.451	0.0101

TABLE VI: Cross sections for the reducible background to single-top production in leptonic channel and for  $b$ -mistagged events,  $\delta\sigma_{\text{mis}} = \sigma_c/10 + \sigma_q/100$ , with cuts  $L_4$  from (11).

where  $c$  stands for  $c$  or  $\bar{c}$ ,  $q$  for any of the quarks or antiquarks lighter than  $c$  and  $\ell, \nu$  are as in (10). The processes in (12) involve 96 diagrams with a charm final state, and 288 diagrams with lighter flavors, for a total of 384 diagrams with four electroweak vertices each. We take the mistagging probability to be 0.1 for  $c$  and 0.01 for  $q$ . Thus, the associated systematical error is given in terms of the cross sections for the processes (12) by  $\delta\sigma_{\text{mis}} = \sigma_c/10 + \sigma_q/100$ . The results for reducible-background cross sections are given in Table VI. Comparing with the signal cross sections given in Table V we obtain mistagging errors of  $\sim 0.65\%$  at the three energies  $E_e = 60, 140$  and  $300$  GeV.

We have considered also the contributions of final states with one additional neutrino pair  $\nu\bar{\nu}$  ( $\nu = \nu_{e,\mu,\tau}$ ), which are found to be negligibly small, as expected. For the signal and irreducible background processes (10), their contribution is less than 0.1% of the cross sections  $\sigma_S$  and  $\sigma_B$  with cuts  $L_4$  in Table V. Reducible background processes of the form (12) with one additional neutrino pair are given by 16968 diagrams (4242 with a charmed final state and 12726 with lighter flavors), with six electroweak vertices. Their contribution to the mistagging cross section  $\delta_{\text{mis}}\sigma$  is less than 0.1% than that in Table VIII. Thus, we disregard final states with additional neutrino pairs in what follows.

We can estimate the statistical error associated to the SM signal from Table V as  $\delta\sigma_{\text{stat}} = \sqrt{\sigma_S/\mathcal{L}}$ , with  $\mathcal{L} = 100 \text{ fb}^{-1}$ . The systematical errors originating in the irreducible background and the mistagging cross section have been given in Tables V and VI. Adding those errors in quadrature we find total errors of 1.7%, 1.9% and 2.3% at  $E_e = 60, 140$  and  $300$  GeV, respectively. As seen from the tables, whereas the three errors  $\delta\sigma_{\text{stat}}$ ,  $\sigma_B$  and  $\delta\sigma_{\text{mis}}$  at  $E_e = 60$  GeV have similar sizes, at 140 and especially at 300 GeV, the dominant source of error in this channel is the irreducible background. From these results, and taking into account other unspecified sources of measurement error, we estimate a lower bound of 3% on experimental errors in the leptonic channel. In what follows we will assume experimental uncertainties of 3%, 6% and 8%.

In order to gain some perspective on the plausibility of these assumed experimental-error levels

for the detection of single top events at the LHeC, we should bear in mind that the latest CMS analysis of single top events at 8 TeV has already reached errors slightly below 9% [30, 49]. In their case some of the most important contributions to this error are jet energy scale, jet energy resolution, missing  $E_T$  and pileup [30]. As mentioned before, it is expected that the LHeC detector will achieve an outstanding performance in these areas. There will be an absence of pileup and in contrast to the single top measurement at the LHC, there is no  $t\bar{t}$  background to take into consideration at the LHeC. Thus, assuming an 8% uncertainty at the LHeC corresponds to the least-favorable scenario in which it barely manages to improve on the precision already achieved by CMS in 2014. As for the feasibility of the minimum of 3%, we point out that the CMS and ATLAS collaborations have reached errors as low as 4.1% and 3.9%, resp., in the measurement of  $\sigma(t\bar{t})$  at  $\sqrt{s} = 7$  TeV in the dileptonic  $\mu e$  mode, and at  $\sqrt{s} = 8$  TeV both collaborations have also reached similarly low errors [49, 50].

For electron polarizations  $\mathcal{P}_e$  up to 90%, the error estimates above do not change significantly. The SM cross section  $\sigma_S$  for the signal process (10) depends on electron polarization as  $\sigma_S(\mathcal{P}_e) = (1 - \mathcal{P}_e)\sigma_S(0)$ ,  $-1 \leq \mathcal{P}_e \leq 1$ . Thus, for the absolute statistical error we have  $\delta\sigma_{\text{stat}}(\mathcal{P}_e) = \sqrt{1 - \mathcal{P}_e} \delta\sigma_{\text{stat}}(0)$ . The irreducible-background cross section  $\sigma_B(\mathcal{P}_e)$  does not tend to zero as  $\mathcal{P}_e \rightarrow 1$ , even for a massless electron, due to the diagrams in Figure 3 in which the  $e^-$  fermion line is attached to the diagram by a  $\gamma/Z$  vertex. The value of  $\sigma_B(+1)$  is very small, however, being 0.04, 0.13, 0.23 fb at  $E_e = 60, 140$  and 300 GeV respectively. Therefore, for moderate right-handed polarization values, the irreducible background cross section scales with  $\mathcal{P}_e$  as  $\sigma_B(\mathcal{P}_e) = (1 - \mathcal{P}_e)\sigma_B(0)$  to a good approximation. Analogous considerations hold for the  $b$ -mistagging cross section  $\delta\sigma_{\text{mis}}$ . By adding the statistical and systematical background errors in quadrature we find for  $\mathcal{P}_e = 0.4$  total errors of 1.8%, 1.9% and 2.3% at  $E_e = 60, 140$  and 300 GeV, respectively. For  $\mathcal{P}_e = 0.7$  the errors are found to be 2.1%, 2.1% and 2.4% at those same electron energies. Thus, for right-handed polarization up to  $\sim 90\%$ , we estimate experimental errors to be in the same range 3–6% as in the unpolarized case.

## B. Standard Model: Hadronic channel

In the hadronic mode the signal ( $S$ ) and signal plus irreducible background ( $S + B$ ) in the SM are defined as

$$S : e^- p(\bar{b}) \rightarrow \bar{t}\nu_e \rightarrow \bar{b}j_u j_d \nu_e, \quad S + B : e^- p(\bar{b}) \rightarrow \bar{b}j_u j_d \nu_e, \quad (13)$$

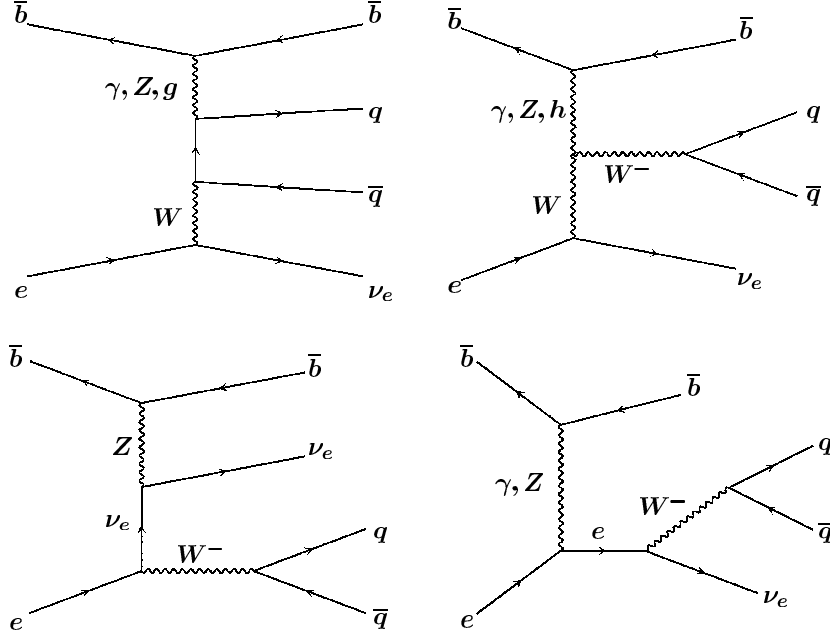


FIG. 4: Feynman diagram for the irreducible background in hadronic-channel single-top production.

where  $j_u = u, c, \bar{u}, \bar{c}$  and  $j_d = d, s, \bar{d}, \bar{s}$ . In the SM the signal process  $S$  involves only two Feynman diagrams, corresponding to Figure 2 with  $f_1, f_2 = \bar{u}, d$  and  $\bar{c}, s$ . The irreducible background  $B$  comprises 24 diagrams: 20 of them with four electroweak vertices and no QCD vertex (like the signal diagram), and 4 diagrams with two QCD vertices and two electroweak vertices, see Figure 4. For the computation of the cross section we impose on the final-state momenta a set of appropriate phase-space cuts. As in the previous section, we consider several progressively more restrictive cuts defined as

$$\begin{aligned}
 H_1 : & \quad |\vec{p}_T(j)| > 20 \text{ GeV}, |\vec{p}_T(\bar{b})| > 20 \text{ GeV}, \\
 H_2 : & \quad H_1, \cancel{E}_T > 25 \text{ GeV}, \\
 H_3 : & \quad H_2, |\eta(j)| < 2.5, |\eta(\bar{b})| < 2.5, \\
 H_4 : & \quad H_3, \Delta R(j, \bar{b}) > 0.4, \Delta R(j, j) > 0.4,
 \end{aligned} \tag{14}$$

with  $\Delta R$  as in (11). The cuts (14) are standard centrality and isolation cuts, needed to ensure a hard partonic scattering and to render the background processes free from infrared instabilities due to the emission of massless quarks. In the cut  $H_3$  we could have set the limit on light-jet pseudorapidity to  $|\eta(j)| < 5$ , given the wide acceptance expected of hadronic calorimeters; we use instead a tighter cut for reasons explained in detail in Appendix B below. Furthermore, in all cases

	$E_e = 60 \text{ GeV}$			$E_e = 140 \text{ GeV}$			$E_e = 300 \text{ GeV}$		
Cuts	$\sigma_S$	$\sigma_B$	$\sigma_{S+B}$	$\sigma_S$	$\sigma_B$	$\sigma_{S+B}$	$\sigma_S$	$\sigma_B$	$\sigma_{S+B}$
$\emptyset$	1.0880			3.280			7.345		
$H_1$	0.7594	0.0059	0.7606	2.284	0.0171	2.287	5.111	0.0372	5.114
$H_2$	0.5590	0.0042	0.5599	1.767	0.0128	1.769	4.063	0.0288	4.069
$H_3$	0.3932	0.0022	0.3941	1.553	0.0101	1.555	3.823	0.0255	3.827
$H_4$	0.3912	0.0022	0.3921	1.545	0.0100	1.546	3.801	0.0252	3.804

TABLE VII: Cross sections in pb for the signal  $S$  and signal-plus-background  $S + B$  processes defined in (13), with the cuts (14) and (15).  $\emptyset$  refers to the cross sections without cuts.

$H_{1,\dots,4}$  we impose the additional cuts

$$\left| \sqrt{(p_{q_1}^2 + p_{q_2}^2 + p_b^2)} - m_t \right| < 15\Gamma_t \quad \text{and} \quad \left| \sqrt{(p_{q_1}^2 + p_{q_2}^2)} - m_W \right| < 15\Gamma_W, \quad (15)$$

where  $q_{1,2}$  refers to the light quarks in the final state. In Table VII we report the effects of the cuts (14), together with (15), on the SM signal, background and total cross sections. Comparing  $\sigma_S + \sigma_B$  with  $\sigma_{S+B}$  from the Table shows that a small interference remains after the cuts (15) have been applied, although at a lower level than in the leptonic channel. We choose the larger ratio  $\sigma_B/\sigma_S$ , rather than  $(\sigma_{S+B} - \sigma_S)/\sigma_S$ , as a measure of the systematical error caused by the irreducible background. That choice turns out to be immaterial in this case, however, since the systematical error is dominated by the reducible background discussed next.

The main source of reducible background in this channel is  $b$ -mistagging in the processes

$$e^- p \rightarrow jjj\nu_e, \quad (16)$$

where  $j$  stands for a gluon or any of the quarks or antiquarks lighter than  $b$ , and  $\nu$  for any of the three neutrino flavors. The processes in (16) involve 528 diagrams in total, of which 128 contain two QCD vertices and two electroweak ones, and 400 contain four electroweak vertices like the signal process  $S$  in (13). The diagrams containing two strong vertices contribute about 80% of the total cross section for (16), whereas the more numerous purely electroweak diagrams supply the remaining 20%. As in the previous section, we take the mistagging probability to be 1/10 for  $c$  and 1/100 for lighter jets. Thus, we have to consider separately out of the reactions (16) those leading to 0, ..., 3 final-state charm quarks. The cross sections for those processes are summarized in Table VIII with the cuts  $H_4$  from (14). In this case we apply a modified version of (15) in which the second equality in that equation must be satisfied by at least one of the three possible pairs of final-state quarks. Given the probability to mistagging as  $b$  a single  $c$  quark and a single lighter

$E_e$ [GeV]	$j_c j_c j_c \nu_e$	$j_c j_c j \nu_e$	$j_c j j \nu_e$	$j j j \nu_e$	$bbj \nu_e$
60	0.0005	0.0085	0.0944	0.2413	0.0111
140	0.0016	0.0228	0.3386	0.6460	0.0263
300	0.0036	0.0451	0.7719	1.2700	0.0473

TABLE VIII: Cross section in pb for reducible-background processes, with phase-space cuts  $H_4$  defined in (14) and (15).

prob. of mistagging	$j_c$	$j_c$	$j$	$j_c$	$j$	$j$
out of	$j_c j_c j_c$	$j_c j_c j$	$j_c j_c j$	$j_c j j$	$j_c j j$	$j j j$
$P$	0.243	0.1782	0.0081	0.09801	0.01782	0.029403

TABLE IX: Probability of mistagging as  $b$  one parton out of the indicated final states, given that the probability of mistagging a  $c$  quark is  $1/10$ , and a lighter parton  $1/100$ .

parton, we have the mistagging probabilities for the three-jet final state shown in Table IX. Also included in Table VIII is the cross section for the final state  $bbj\nu$  [51] which, assuming a  $b$ -tagging efficiency of 60%, has a probability of 0.48 of being mistagged as  $bjj\nu$ .

By combining the results of Table VIII and IX we get mistagging cross sections  $\delta\sigma_{\text{mis}} = 25.1, 75.5$  and  $158.7$  fb at  $E_e = 60, 140, 300$  GeV, respectively. We remark that with the cuts  $H_4$  as defined in (14), but without the cuts (15), the mistagging cross sections would be  $131.4, 424.9$  and  $998.6$  fb at  $E_e = 60, 140, 300$  GeV, respectively, corresponding to  $\sim 30\%$  of the signal cross section. It is the top-mass cut given by the first equality in (15) that plays a crucial role in taming this large reducible background.

Processes with additional neutrino pairs in the final state yield negligible cross sections, as expected. Indeed, the cross section for signal and irreducible background processes of the form (13) with one additional neutrino pair in the final state are less than  $0.1\%$  of  $\sigma_S$  and less than  $1\%$  of  $\sigma_B$  as given in Table VII. The reducible background processes (16) with an additional final-state neutrino pair yield a scattering amplitude with 144 diagrams for three- $c$  final states, 432 for two- $c$ , 1360 for one- $c$  and 2432 for no- $c$  final states. Computation of the cross section in this case, with cuts  $H_4$ , gives results that are less than  $0.1\%$  of those in Table VIII. Thus, we ignore processes with multi-neutrino final states in what follows.

As stated at the beginning of this section, we assume a total integrated luminosity  $\mathcal{L} = 100 \text{ fb}^{-1}$ . Thus, for the statistical error associated to the SM signal from Table VII we get  $\delta\sigma_{\text{stat}} = 2, 3.9, 6.2$  fb at  $E_e = 60, 140, 300$  GeV, respectively. We consider the  $b$ -mistagging cross section given above and the irreducible background  $\sigma_B$  from Table VII as systematical errors. It is apparent from these

results that the dominant source of error in this channel is the reducible background. By adding statistical and systematical errors in quadrature we find total errors of 6.4%, 4.9% and 4.2% at  $E_e = 60, 140$  and  $300$  GeV, respectively, relative to the signal cross sections with cuts  $H_4$  from Table VII. From this evaluation of statistical and background errors, and taking into account other unspecified sources of measurement error, we estimate a lower bound of 7% on the experimental error. We cannot use existing experimental results on single-top production as guidelines in our error estimates, since the hadronic channel has never been observed so far. We notice, however, that the cross section for  $t\bar{t}$  production in the semileptonic channel has been measured by CMS at  $\sqrt{s} = 7$  TeV [52] with an error of 7%, and by ATLAS at  $\sqrt{s} = 8$  TeV with an error of 13% [53]. Therefore, we believe that experimental errors in the range 7–12% for the hadronic channel could be achieved at the LHeC.

If the electron beam is polarized, the SM cross section  $\sigma_S$  for the signal process (13) depends on electron polarization as  $\sigma_S(\mathcal{P}_e) = (1 - \mathcal{P}_e)\sigma_S(0)$ ,  $-1 \leq \mathcal{P}_e \leq 1$ , as is apparent from Figure 2. Thus, for the statistical error we have  $\delta\sigma_{\text{stat}}(\mathcal{P}_e) = \sqrt{1 - \mathcal{P}_e} \delta\sigma_{\text{stat}}(0)$ . For a massless electron, the dependence of the irreducible-background cross section  $\sigma_B$  with  $\mathcal{P}_e$  is the same as that of the signal cross section, as can be seen from Figure 4, so  $\sigma_B(\mathcal{P}_e)/\sigma_S(\mathcal{P}_e) = \sigma_B(0)/\sigma_S(0)$ . The same considerations hold for the reducible background (16). Our results for the systematical error originating in background processes in the unpolarized case, therefore, remain unchanced in the polarized case when expressed as a fraction of the signal cross section. Since the statistical-error contribution to the total error is much smaller than that of the reducible background, the variation of  $\delta\sigma_{\text{stat}}$  with  $\mathcal{P}_e$  will not significantly change our estimate of the total error as long as it remains subdominant relative to  $\delta\sigma_{\text{mis}}$ . Thus, for  $\mathcal{P}_e \lesssim +0.9$  we consider experimental errors in the same range 7-12% as in the unpolarized case.

### C. Theoretical uncertainties

The computations of the SM cross sections for single-antitop production and decay are affected by theoretical uncertainties that we briefly discuss here. The use of LO PDFs leads to uncertainties arising from the choice of renormalization and factorization scales that we estimate by varying them as  $\mu_R = \mu_F = m_t/2, m_t, 2m_t$ . The scale uncertainty in the unpolarized cross section is found to be 7.5%, 9%, 10.3% at  $E_e = 60, 140, 300$  GeV for both the leptonic and the hadronic channel. The choice of PDF is also a source of uncertainty, which we have found to be 2%, 5%, 6% for both channels at the same three energies. The NLO correction to the LO approximation depicted in

Figure 2 has not yet been given in the literature, but it could be of order 3% as in the t-channel top production at the LHC [54]. We emphasize here, however, that these theoretical uncertainties have only a minor impact on the results presented in this paper. This is so because the bounds and exclusion regions for effective couplings presented in sections III and V depend on cross sections only through the ratio  $R = \sigma_{\text{eff}}(\lambda)/\sigma_{\text{eff}}(0)$ , with  $\sigma_{\text{eff}}(\lambda)$  the tree-level cross section in the effective theory, depending on the effective couplings  $\lambda$ , and  $\sigma_{\text{eff}}(\lambda = 0)$  the tree-level SM cross section. For values of the effective couplings within the bounds established below, we find the scale and PDF uncertainties in the ratio  $R$  to be  $\lesssim 0.6\%$ . Notice that this uncertainty is significantly smaller than the experimental errors assumed in the two previous subsections.

## V. CONTRIBUTION FROM THE EFFECTIVE OPERATORS

For the computation of the amplitudes in the effective theory we make the same approximations—i.e., two massless generations and diagonal CKM matrix—and the same choices of parameters, PDF and scales as in the SM calculations of section IV. We implemented the basis of dimension-six  $SU(2)_L \times U(1)$ -invariant effective operators involved in the anomalous  $tbW$  couplings and contact-interaction vertices in MADGRAPH 5 by means of the program FEYNRULES 2.0 [55].

The full set of tree-level Feynman diagrams for single-top production (including the top decay) in  $ep$  collisions is given by the SM diagram from Figure 2 together with the diagrams in Figure 5. There can be one or two effective vertices of the  $SU(2)_L \times U(1)$  gauge-invariant effective theory. Diagrams with two effective vertices must be taken into account, as they contribute with terms of second order that come from the interference with the SM amplitude. Thus, the cross section numerical expressions contain terms of up to fourth order in the effective couplings. However, it turns out that within the bounds obtained below, the contributions from terms of order higher than the second are negligibly small. Below, we show the single antitop production cross section ratio at the LHeC without terms of third and fourth order:

$$\frac{\sigma^{\text{SM}} + \Delta\sigma}{\sigma_{V_L=1}^{\text{SM}}} = (1 + \delta V_L)^4 + b_{12}g_R^r + b_2g_R^{r2} + d_2g_R^{i2} + b_{13}V_R^r + b_3V_R^{r2} + d_3V_R^{i2} + b_{14}g_L^r + b_4g_L^{r2} + d_4g_L^{i2} + b_{15}C_1 + b_5C_1^2 + b_6C_2^r + d_6C_2^{i2} + b_7C_3^{r2} + d_7C_3^{i2} + b_8C_4^r + d_8C_4^{i2} . \quad (17)$$

Unlike the previous simple expression in Eq. (9), here we have assumed that the effective coefficients are complex numbers, except  $V_L = 1 + \delta V_L$  and  $C_1$  [17]. For a given complex coupling  $\lambda$  we denote its real and imaginary parts as  $\lambda = \lambda^r + i\lambda^i$ . The coefficients in (17) for the leptonic- and hadronic-

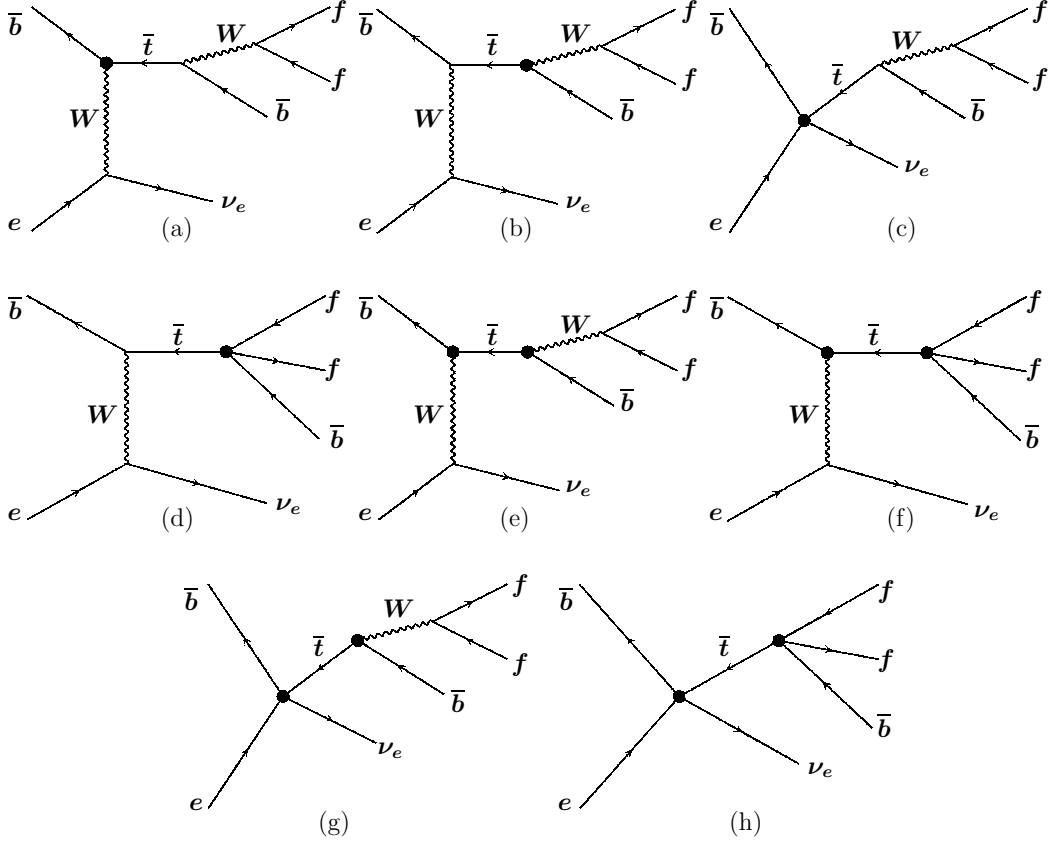


FIG. 5: Feynman diagrams for single-top production and decay in  $ep$  collisions containing one or two effective vertices. The  $W^-$ -decay products  $f$  can be  $e, \bar{\nu}_e$  or  $\mu, \bar{\nu}_\mu$  in the leptonic channel, and  $\bar{u}, d$ , or  $\bar{c}, s$  in the hadronic channel.

channel cross sections, with unpolarized and polarized electron beams, are given in Appendix A. Notice that the coefficients of the  $tbW$  couplings in (17) are larger than the ones in (9), but the coefficients of the contact-interaction couplings have roughly the same values in both cases, due to the effect of the anomalous  $tbW$  couplings on the decay vertex which is not taken into account in the preliminary analysis of section III B. Thus, as expected, the bounds on  $tbW$  couplings obtained in this section are stronger than the ones in section III. Notice also that  $b_{13}$  and  $b_{14}$  are small compared to  $b_{12}$  because of the  $m_b$  suppression. For simplicity, we do not include in (17) interference terms involving two different effective couplings. This is appropriate with the goal of obtaining bounds by taking only one coupling non-zero at a time. On the other hand, we do take into account all interference terms involving two anomalous couplings for the computation of the correlated regions of allowed parameter space discussed below.

In addition to the total cross section  $\sigma$  we consider various asymmetries  $A(X, X_0)$ , where  $X$  is the kinematical observable and  $X_0$  the reference value:  $A(X, X_0) =$



$\left(\sigma(X > X_0) - \sigma(X < X_0)\right) / \left(\sigma(X > X_0) + \sigma(X < X_0)\right)$ . In what follows, when the reference value is  $X_0 = 0$  we simply write  $A(X) \equiv A(X, 0)$ .

Polarization of the electron beam does not change the sensitivity of the cross-section ratios in (17), or in the various asymmetries, to the couplings in the  $tbW$  Lagrangian (3), as the  $\nu eW$  vertex in Figure 5 is always the same as in the SM. For the same reason, it cannot change the sensitivity to the contact-interaction coupling  $C_1$  multiplying the operator  $O_{\ell q}^{1331}$  in the Lagrangian (1), as the electron there is left-handed. The couplings  $C_{2,3,4}$ , on the other hand, involve a right-handed electron. The sensitivity of the cross section and the asymmetries to those couplings is then strongly enhanced by right-polarization of the electron beam, as discussed in detail in the remainder of this section.

### A. Bounds from leptonic channel

In the leptonic channel, due to the presence of two neutrinos in the final state, the kinematics of the reaction cannot be fully determined experimentally. In particular, the four-momenta of final-state charged particles can only be determined in the lab frame, and the momenta of the intermediate-state  $\bar{t}$ ,  $W^-$  and of the initial-state  $\bar{b}$  cannot be reconstructed. The only experimentally accessible quantities are the four-momenta of  $\bar{b}$ ,  $\ell$ , the missing energy  $\cancel{E}_T = |\vec{p}_{T\nu_e} + \vec{p}_{T\bar{\nu}}|$  and its azimuthal angle  $\varphi(\cancel{E}_T)$ . The observables we consider are the cross section  $\sigma$  and the asymmetries associated with  $\Delta\eta(\bar{b}, \ell)$ ,  $\Delta\varphi(\bar{b}, \ell)$ ,  $\Delta\varphi(\bar{b}, \cancel{E}_T)$ ,  $\Delta\varphi(\ell, \cancel{E}_T)$ ,  $\cos(\bar{b}, \ell)$ , and the leptonic fraction of the visible energy  $u(\bar{b}, \ell) = E_\ell / (E_\ell + E_{\bar{b}})$  [56]. All of these kinematic variables refer to the lab frame, although  $\Delta\eta$ ,  $\varphi$  and  $\Delta\varphi$  are obviously invariant under longitudinal boosts. We compute all cross sections and asymmetries with the cuts  $L_4$  defined in (11).

Despite their not being shown in Eq. (17), the contributions from terms cubic and quartic in the effective  $tbW$  and contact-interaction couplings have been fully taken into account in our computation of anomalous-coupling bounds. These contributions are at least one order of magnitude smaller than the quadratic terms for the  $tbW$  couplings within the bounds obtained below. For the contact terms they are even smaller, as contact-interaction effects on the decay vertex are insignificant [35].

In Table X we report the bounds on effective couplings obtained from the unpolarized cross section at the level of one standard deviation, assuming experimental errors of 3% and 6% as discussed in section IV A. As seen in the table, the sensitivity to the  $tbW$  couplings and the contact interactions is not very dependent on  $E_e$ . Notice also that the coefficients for Eq. (17)

	$\epsilon_{\text{exp}} = 3\%$			$\epsilon_{\text{exp}} = 6\%$		
	60 GeV	140 GeV	300 GeV	60 GeV	140 GeV	300 GeV
$\delta V_L \times 10^2$	-0.76 0.73	-0.76 0.73	-0.76 0.76	-1.55 1.48	-1.55 1.45	-1.55 1.48
$V_R^r \times 10$	-0.96 1.21	-0.98 1.25	-0.98 1.28	-1.40 1.66	-1.43 1.69	-1.45 1.73
$V_R^i \times 10$	-1.09 1.09	-1.12 1.12	-1.12 1.12	-1.53 1.53	-1.57 1.57	-1.58 1.58
$g_R^r \times 10$	-0.21 0.22	-0.22 0.23	-0.22 0.23	-0.42 0.45	-0.43 0.48	-0.43 0.49
$g_R^i \times 10$	-1.11 1.11	-1.05 1.05	-1.02 1.02	-1.56 1.56	-1.49 1.49	-1.44 1.44
$g_L^r \times 10$	-0.97 0.72	-0.96 0.72	-0.96 0.72	-1.30 1.05	-1.30 1.06	-1.30 1.05
$g_L^i \times 10$	-0.83 0.83	-0.83 0.83	-0.83 0.83	-1.17 1.17	-1.17 1.17	-1.17 1.17
$C_1$	-0.24 0.25	-0.22 0.23	-0.20 0.21	-0.47 0.50	-0.44 0.46	-0.40 0.43
$C_2^{r,i}$	-4.06 4.06	-3.60 3.60	-3.16 3.16	-5.74 5.74	-5.09 5.09	-4.47 4.47
$C_3^{r,i}$	-2.43 2.43	-2.08 2.08	-1.80 1.80	-3.44 3.44	-2.95 2.95	-2.55 2.55
$C_4^{r,i}$	-3.83 3.83	-3.45 3.45	-3.04 3.04	-5.43 5.43	-4.88 4.88	-4.30 4.30

TABLE X: Bounds on effective couplings at the 68% CL obtained from the leptonic-channel unpolarized cross section by varying the couplings one at a time. The assumed experimental errors are 3% and 6%.

shown in the appendix change little with the three electron energies. This is because the energy of the collision goes as  $\sqrt{s} = \sqrt{4E_e E_p} = 1.3, 2.0$  and  $2.9$  TeV which does not increase with the same proportion as  $E_e$ . The allowed ranges for the imaginary parts of the anomalous  $tbW$  couplings are symmetric about 0 due to the absence of interference of those couplings with the SM. In the case of the contact-interaction couplings  $C_{2,3,4}$ , whose real parts do not interfere with the SM, the allowed ranges for the imaginary parts  $C_{2,3,4}^i$  are equal to those for the real parts  $C_{2,3,4}^r$ . We remark here, as done in Section III, that the difference in order of magnitude between the bounds for the  $tbW$  form factors and those for the contact-interaction couplings is due to a large extent to the normalization of the former. Indeed, using for example the results for  $\delta V_L$  from Table X together with (6), we get  $-0.25 < C_{\phi q} < 0.24$ , to be compared with the bounds for  $C_1$  given in the table which are essentially the same.

For the contact-interaction couplings  $C_{2,3,4}$ , which involve right-handed electrons, the bounds given in Table X can be significantly improved if the electron beam is right polarized. In Table XI we give the bounds obtained for those couplings by assuming the initial-electron polarizations  $\mathcal{P}_e = +0.4$  and  $+0.7$ . As discussed in section IV A, the experimental errors for those polarizations are expected to be in the same range as in the unpolarized case.

As mentioned above, besides the cross section we have considered as well several asymmetries. In the leptonic channel asymmetries turn out not to possess much better sensitivity than the cross

		$\epsilon_{\text{exp}} = 3\%$			$\epsilon_{\text{exp}} = 6\%$		
		60 GeV	140 GeV	300 GeV	60 GeV	140 GeV	300 GeV
$\mathcal{P}_e = 0.4$	$C_2^{r,i}$	$\pm 2.66$	$\pm 2.36$	$\pm 2.07$	$\pm 3.76$	$\pm 3.34$	$\pm 2.93$
	$C_3^{r,i}$	$\pm 1.59$	$\pm 1.36$	$\pm 1.18$	$\pm 2.25$	$\pm 1.93$	$\pm 1.67$
	$C_4^{r,i}$	$\pm 2.54$	$\pm 2.26$	$\pm 1.99$	$\pm 3.59$	$\pm 3.20$	$\pm 2.81$
$\mathcal{P}_e = 0.7$	$C_2^{r,i}$	$\pm 1.71$	$\pm 1.52$	$\pm 1.32$	$\pm 2.41$	$\pm 2.14$	$\pm 1.87$
	$C_3^{r,i}$	$\pm 1.02$	$\pm 0.87$	$\pm 0.76$	$\pm 1.45$	$\pm 1.24$	$\pm 1.07$
	$C_4^{r,i}$	$\pm 1.63$	$\pm 1.45$	$\pm 1.28$	$\pm 2.30$	$\pm 2.05$	$\pm 1.81$

TABLE XI: Bounds at the 68% CL on contact-interaction couplings involving initial right-handed electrons, obtained from the leptonic-channel polarized cross section by varying the couplings one at a time. The assumed experimental errors are 3% and 6%.

section to anomalous couplings. For  $\delta V_L$ ,  $g_L$  and  $C_1$  the cross section is the only observable having significant sensitivity. Of the six asymmetries we considered, only three yielded better bounds on some coupling than the cross section. The asymmetry  $A(\Delta\eta(\bar{b}, \ell))$  yields significantly tighter bounds on  $C_2$ , and slightly tighter bounds on  $V_R$  and  $g_R$ . The bounds on  $C_3$  from this observable are the same as those from the cross section.  $A(\Delta\varphi(\bar{b}, \ell), \pi/2)$  improves the bounds on  $C_3$  and  $C_4$ , and  $A(\Delta\varphi(\ell, \cancel{E}_T), \pi/2)$  improves the bounds on  $C_3$ . In Table XII we summarize the bounds on the effective couplings obtained from asymmetries, including only those results that are as restrictive or better than the corresponding results in Table X. As in the case of the total cross section, the sensitivity of the asymmetries to the couplings  $C_{2,3,4}$ , involving right-handed initial electrons, can be significantly enhanced by assuming a right-polarized electron beam. In Table XIII we summarize our results on these couplings, using the same asymmetries as in Table XII, with initial electron polarizations  $\mathcal{P}_e = +0.4$ ,  $+0.7$ , and with the same range of assumed experimental errors.

The asymmetry of  $\Delta\varphi(\bar{b}, \cancel{E}_T)$ , with reference value  $\pi/2$ , has only some marginal sensitivity to  $C_3$  leading to bounds much weaker than those in Table XII. Similarly, the asymmetry related to  $\cos(\bar{b}, \ell)$  leads to loose bounds on  $C_3$ ,  $g_R$ ,  $g_L$ . We considered also the asymmetry  $A(u(\bar{b}, \ell), u_0)$  with  $u_0 = m_W^2/m_t^2 \simeq 0.215$ , where the distribution of  $u$  has a shoulder [56], and also with  $u_0 = 1/2$ . The former reference value yields better result than the latter, but even in that case we do not find this asymmetry to possess any significant sensitivity to the effective couplings studied in this paper, at the energies considered here. For instance, for the coupling  $C_1$  we find the marginally interesting bounds  $-4.8 < C_1 < 8.4$  at  $\epsilon = 3\%$  and  $-11.1 < C_1 < 9.5$  at  $\epsilon = 6\%$ , which are much weaker than the bounds from the unpolarized cross section.

We have also studied the sensitivity of single top production in the leptonic channel to the four-

Observable		$\epsilon_{\text{exp}} = 3\%$			$\epsilon_{\text{exp}} = 6\%$		
		60 GeV	140 GeV	300 GeV	60 GeV	140 GeV	300 GeV
$V_R^r \times 10$	$\Delta\eta(\bar{b}, \ell)$	-0.93 0.89	-0.92 0.94	-0.96 0.97	-1.31 1.28	-1.32 1.34	-1.38 1.39
$V_R^i \times 10$	$\Delta\eta(\bar{b}, \ell)$	-0.92 0.92	-0.94 0.94	-0.95 0.95	-1.32 1.32	-1.35 1.35	-1.36 1.36
$g_R^r \times 10$	$\Delta\eta(\bar{b}, \ell)$	-0.20 0.19	-0.18 0.18	-0.18 0.17	-0.39 0.38	-0.38 0.35	-0.36 0.33
$g_R^i \times 10$	$\Delta\eta(\bar{b}, \ell)$	-0.82 0.82	-0.79 0.79	-0.76 0.76	-1.17 1.17	-1.13 1.13	-1.09 1.09
$C_2^{r,i}$	$\Delta\eta(\bar{b}, \ell)$	-2.83 2.83	-2.63 2.63	-2.38 2.38	-4.04 4.04	-3.75 3.75	-3.40 3.40
$C_3^{r,i}$	$\Delta\varphi(\bar{b}, \ell)$	-2.18 2.18	-1.56 1.56	-1.21 1.21	-3.11 3.11	-2.22 2.22	-1.72 1.72
	$\Delta\varphi(\ell, \cancel{E}_T)$	-2.35 2.35	-2.05 2.05	-1.76 1.76	-3.37 3.37	-2.95 2.95	-2.53 2.53
	$\Delta\eta(\bar{b}, \ell)$	-2.43 2.43	-2.11 2.11	-1.82 1.82	-3.49 3.49	-3.03 3.03	-2.61 2.61
$C_4^{r,i}$	$\Delta\varphi(\bar{b}, \ell)$	-3.72 3.72	-2.75 2.75	-2.13 2.13	-5.34 5.34	-3.92 3.92	-3.03 3.03

TABLE XII: Bounds on effective couplings at the 68% CL obtained from the indicated leptonic-channel unpolarized asymmetries by varying the couplings one at a time.  $\Delta\eta(\bar{b}, \ell)$  stands for the asymmetry  $A(\Delta\eta(\bar{b}, \ell), 0)$ ,  $\Delta\varphi(\bar{b}, \ell)$  for  $A(\Delta\varphi(\bar{b}, \ell), \pi/2)$  and  $\Delta\varphi(\ell, \cancel{E}_T)$  for  $A(\Delta\varphi(\ell, \cancel{E}_T), \pi/2)$ . The assumed experimental errors are 3% and 6%.

Observable		$\epsilon_{\text{exp}} = 3\%$			$\epsilon_{\text{exp}} = 6\%$			
		60 GeV	140 GeV	300 GeV	60 GeV	140 GeV	300 GeV	
$\mathcal{P}_e = 0.4$	$C_2^{r,i}$	$\Delta\eta(\bar{b}, \ell)$	$\pm 1.87$	$\pm 1.73$	$\pm 1.56$	$\pm 2.66$	$\pm 2.46$	$\pm 2.23$
	$C_3^{r,i}$	$\Delta\varphi(\bar{b}, \ell)$	$\pm 1.42$	$\pm 1.02$	$\pm 0.79$	$\pm 2.04$	$\pm 1.46$	$\pm 1.13$
		$\Delta\varphi(\ell, \cancel{E}_T)$	$\pm 1.54$	$\pm 1.34$	$\pm 1.15$	$\pm 2.21$	$\pm 1.93$	$\pm 1.66$
		$\Delta\eta(\bar{b}, \ell)$	$\pm 1.62$	$\pm 1.39$	$\pm 1.20$	$\pm 2.32$	$\pm 1.99$	$\pm 1.73$
$C_4^{r,i}$	$\Delta\varphi(\bar{b}, \ell)$	$\pm 2.45$	$\pm 1.80$	$\pm 1.40$	$\pm 3.51$	$\pm 2.57$	$\pm 1.99$	
$\mathcal{P}_e = 0.7$	$C_2^{r,i}$	$\Delta\eta(\bar{b}, \ell)$	$\pm 1.20$	$\pm 1.11$	$\pm 1.00$	$\pm 1.72$	$\pm 1.58$	$\pm 1.43$
	$C_3^{r,i}$	$\Delta\varphi(\bar{b}, \ell)$	$\pm 0.91$	$\pm 0.66$	$\pm 0.51$	$\pm 1.30$	$\pm 0.94$	$\pm 0.72$
		$\Delta\varphi(\ell, \cancel{E}_T)$	$\pm 0.99$	$\pm 0.86$	$\pm 0.74$	$\pm 1.42$	$\pm 1.23$	$\pm 1.06$
		$\Delta\eta(\bar{b}, \ell)$	$\pm 1.04$	$\pm 0.89$	$\pm 0.77$	$\pm 1.49$	$\pm 1.28$	$\pm 1.11$
	$C_4^{r,i}$	$\Delta\varphi(\bar{b}, \ell)$	$\pm 1.56$	$\pm 1.15$	$\pm 0.90$	$\pm 2.24$	$\pm 1.64$	$\pm 1.28$

TABLE XIII: Bounds at the 68% CL on contact-interaction couplings involving initial right-handed electrons, obtained from the indicated leptonic-channel asymmetries by varying the couplings one at a time. The definition of the asymmetries is as in table XII. The assumed experimental errors are 3% and 6%.

fermion operators  $\mathcal{O}_{lq'}^{2332}$ ,  $\mathcal{O}_{qde}^{2233}$ ,  $\mathcal{O}_{q\ell\epsilon}^{3223}$ ,  $\mathcal{O}_{lq\epsilon}^{2233}$ , involving second-generation leptons. These operators are obtained from those in Table I by substituting  $e, \nu_e$  by  $\mu, \nu_\mu$ . At the LHeC, these operators can only enter single-top production and decay through the top decay vertex (diagrams (d), (f), (h) in Figure 5). Since the contribution of contact interactions to the top decay vertex is known to

be negligible [35], we do not expect to find any sensitivity to the coupling constants associated to these operators. That is, in fact, the case. The bounds we find on four-fermion couplings involving muons are quite weak, of order  $C \sim 10^2$  (or, equivalently, new physics scales  $\Lambda \gtrsim 100$  GeV).

We should compare the bounds obtained here with those from [9], which are based on a combined bin analysis of the distributions of a similar set of kinematical observables as ours. In particular, from Figure 7 of [9] with 10% systematical error we observe similar bounds for  $\delta V_L$  ( $\simeq 10^{-2}$ ),  $V_R$  and  $g_L$  ( $\simeq 10^{-1}$ ). On the other hand, our bounds on  $g_R$  ( $\simeq 0.02$ ) are somewhat tighter than theirs ( $\simeq 0.03$ ).

We turn next to the allowed regions of parameter space obtained by letting two couplings to be non-zero simultaneously, and by allowing for the necessary additional interference terms in (17). In Figure 6 the allowed regions at 68% confidence level (CL) and at  $E_e = 60$  GeV are shown, on the planes  $\delta V_L - V_R^r$ ,  $g_R^r$ ,  $g_L^r$  and  $C_1$ . In all cases we assume an unpolarized electron beam, as is appropriate for these couplings. In the cases of  $V_R^r$  and  $g_R^r$  (figures 6 (a) and (b)) the allowed regions are determined by the level curves of the asymmetry  $A(\Delta\eta(\bar{b}, \ell))$  and of the cross section. For  $\delta V_L$  and  $g_L^r$  the only available observable with significant sensitivity to both couplings is the cross section. The resulting allowed region is not a neighborhood of the origin, but an elliptical corona having the origin at its periapsis. In order to obtain a neighborhood of the origin, in Figure 6 (c) we used the level curves of the cross section and the asymmetry  $A(\Delta\varphi(\bar{b}, \cancel{E}_T))$ . As a consequence, the single-coupling bounds on  $g_L^r$  determined by the intersection of the allowed region in the figure with the axis  $\delta V_L = 0$  are less restrictive than those obtained directly from the cross section (see Table X). Similarly, for the couplings  $\delta V_L$  and  $C_1$  the only sensitive observable is the cross section  $\sigma$ . For moderate values of these couplings,  $\sigma$  does not depend on them independently but only through a linear combination, as can be seen in Figure 6 (d). Also shown in that figure, for reference, is the current bound  $V_L = 0.998 \pm 0.038$  (exp) from CMS [30].

We determine the allowed region in the plane  $V_R^r - V_R^i$  from the asymmetry  $A(\Delta(\eta(\bar{b}, \ell)))$ , which gives the best bounds on these couplings (see Table XII). Since the interference term with the SM proportional to  $V_R^r$  is small (see Appendix A), the resulting allowed region is essentially a solid ellipse inscribed in the rectangle formed with the single-coupling bounds from  $A(\Delta(\eta(\bar{b}, \ell)))$ . Similarly, the allowed region in the plane  $g_L^r - g_L^i$  is a solid ellipse inscribed in the rectangle determined by the single-coupling bounds given in Table X. A figure for these allowed regions is therefore not needed.

There is a substantial interference term proportional to  $g_R^r$  in (17), however, as shown by its coefficients in Appendix A. Thus the allowed region in the plane  $g_R^r - g_R^i$  determined by the cross

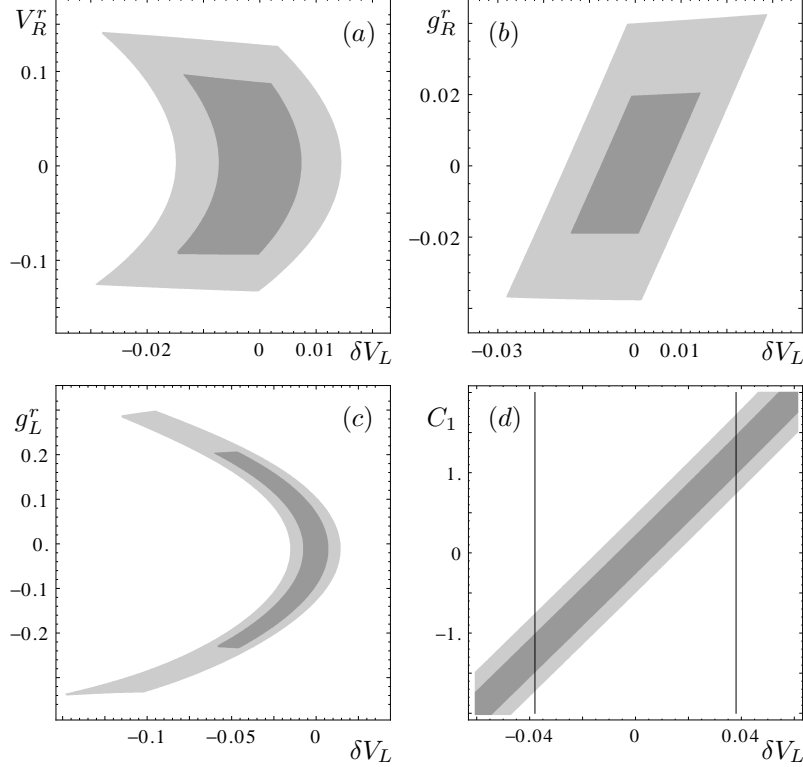


FIG. 6: Allowed regions at 68% CL at  $E_e = 60$  GeV for (a)  $\delta V_L$ ,  $V_R$  from the cross section and the asymmetry  $A(\Delta\eta(\bar{b}, \ell))$ , (b)  $\delta V_L$ ,  $g_R$  from the cross section and the asymmetry  $A(\Delta\eta(\bar{b}, \ell))$ , (c)  $\delta V_L$ ,  $g_L$  from the cross section and the asymmetry  $A(\Delta\varphi(\bar{b}, \ell))$ , (d)  $\delta V_L$ ,  $C_1$  from the cross section. The vertical lines in (d) correspond to the current bounds  $|\delta V_L| < 0.038$  [30]. The light-gray regions correspond to  $\varepsilon_{\text{exp}} = 8\%$ , the medium-gray regions to  $\varepsilon_{\text{exp}} = 6\%$  and the dark-gray regions to  $\varepsilon_{\text{exp}} = 3\%$ .

section alone or the asymmetry  $A(\Delta(\eta(\bar{b}, \ell)))$  alone, are elliptical coronas. In Figure 7 we show the allowed region in the plane  $g_R^r - g_R^i$  resulting from the intersection of the level curves of the cross section and the asymmetries  $A(\Delta\eta(\bar{b}, \ell))$  and  $A(\Delta\varphi(\bar{b}, \ell))$ .

The leptonic cross section and the asymmetry  $A(\Delta\eta(\bar{b}, \ell))$  yield the best bounds on the couplings  $g_L$  and  $V_R$ , respectively, as seen from Tables X and XII. The allowed regions determined by those observables in the planes  $V_R^r - g_L^r$  and  $V_R^i - g_L^i$  are shown in Figure 8. We have taken into account in the figure interference terms of the form  $V_R \times g_L$ , which are not suppressed by  $m_b$ .

The allowed regions for the contact-interaction couplings  $C_{2,3,4}^r$  versus  $C_1$  are shown in Figure 9, at  $E_e = 60$  GeV for electron-beam polarizations  $\mathcal{P}_e = 0.0, +0.4, +0.7$ . The large increase in sensitivity to  $C_{2,3,4}^r$ , already apparent from Tables XI and XIII, is clearly seen in the figure. The figures for  $C_2^i, C_3^i, C_4^i$  versus  $C_1$  are essentially identical to Figure 9.

The best bounds we obtain on  $C_2$  are those from the leptonic-channel asymmetry  $A(\Delta\eta(\bar{b}, \ell))$ ,

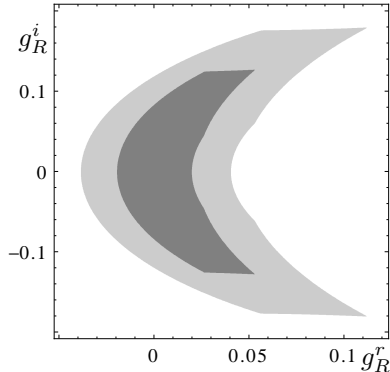


FIG. 7: Allowed regions at 68% CL at  $E_e = 60$  GeV for  $g_R$  obtained from the leptonic cross section and the asymmetries  $A(\Delta\eta(\bar{b}, \ell))$  and  $A(\Delta\varphi(\bar{b}, \ell))$ . The light-gray area corresponds to  $\varepsilon_{\text{exp}} = 8\%$ , the medium-gray one to  $\varepsilon_{\text{exp}} = 6\%$  and the dark-gray one to  $\varepsilon_{\text{exp}} = 3\%$ .

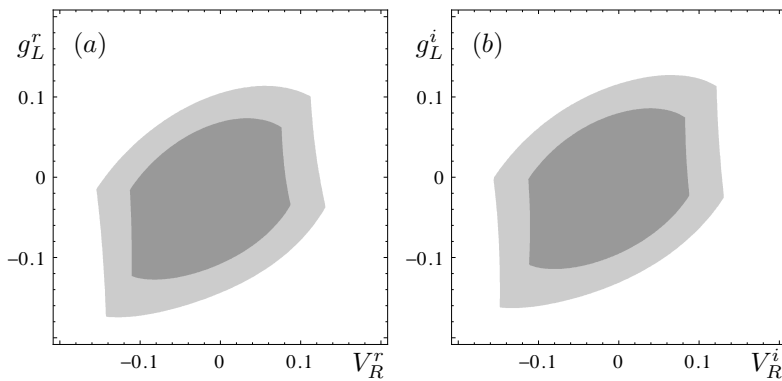


FIG. 8: Allowed regions at 68% CL at  $E_e = 60$  GeV in the plane (a)  $V_R^r - g_L^r$  and (b)  $V_R^i - g_L^i$ , obtained from the asymmetries  $A(\Delta\eta(\bar{b}, \ell))$  and the cross section. The light-gray areas correspond to  $\varepsilon_{\text{exp}} = 8\%$ , the medium-gray ones to  $\varepsilon_{\text{exp}} = 6\%$  and the dark-gray ones to  $\varepsilon_{\text{exp}} = 3\%$ .

and the bounds on  $C_3$  from the leptonic asymmetry  $A(\Delta\varphi(\bar{b}, \ell))$  are equally tight as those obtained in the hadronic channel (see section VB below). The allowed regions in the plane  $C_2^r - C_3^r$  determined by those asymmetries are displayed in Figure 10 for the three electron polarizations  $\mathcal{P}_e = 0.0, +0.4, +0.7$ .

## B. Bounds from hadronic channel

In the hadronic channel it is possible to measure the four-momenta of the three final-state jets and, therefore, to reconstruct the four-momenta of the intermediate-state  $W$  and  $\bar{t}$ . From the known four-momenta of the initial electron and of  $\bar{t}$  the entire kinematics of the process can be fully reconstructed. In particular, we can find the four-momenta of the final-state neutrino and

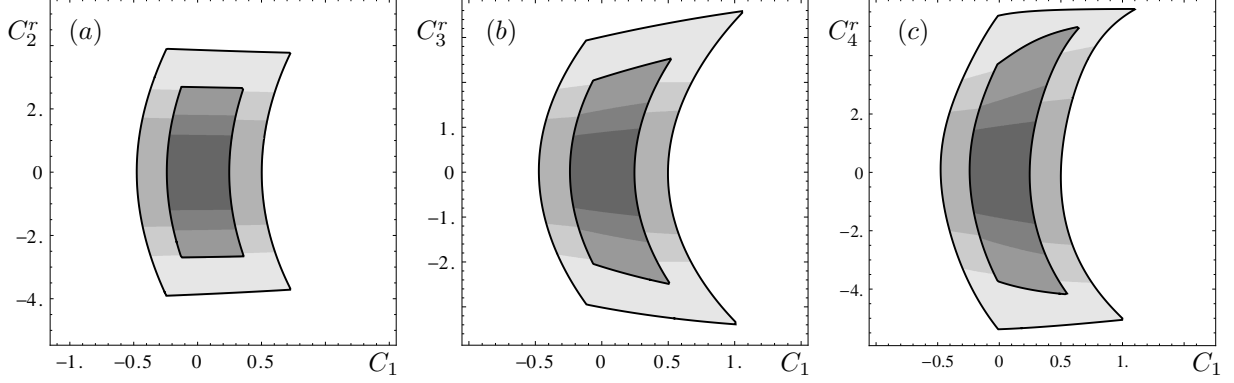


FIG. 9: Allowed regions at 68% CL at  $E_e = 60$  GeV for (a)  $C_1^r$ ,  $C_2^r$  from the unpolarized cross section and the asymmetry  $A(\Delta\eta(\bar{b}, \ell))$ , (b)  $C_1^r$ ,  $C_3^r$  from the unpolarized cross section and the asymmetry  $A(\Delta\varphi(\bar{b}, \ell))$ , (c)  $C_1^r$ ,  $C_4^r$  from the unpolarized cross section and the asymmetry  $A(\Delta\varphi(\bar{b}, \ell))$ . The larger quadrangles in each panel correspond to  $\varepsilon_{\text{exp}} = 6\%$ , the smaller ones to  $\varepsilon_{\text{exp}} = 3\%$ . Within each quadrangle the lighter-gray region corresponds to  $\mathcal{P}_e = 0$ , the medium-gray region to  $\mathcal{P}_e = 0.4$  and the darker-gray region to  $\mathcal{P}_e = 0.7$ .

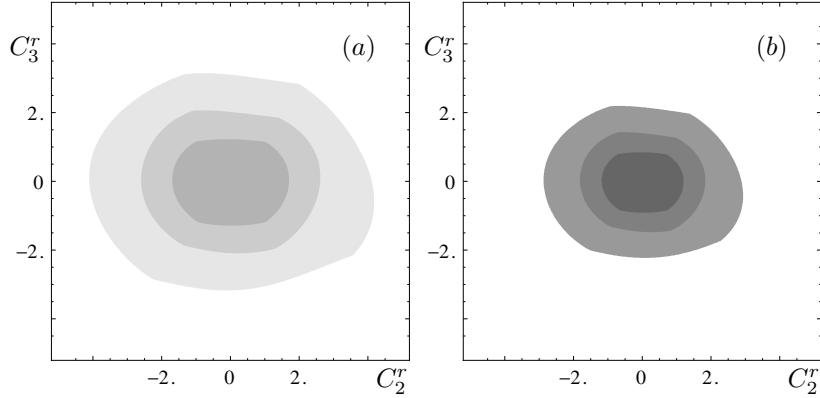


FIG. 10: Allowed regions at 68% CL at  $E_e = 60$  GeV for  $C_2^r$ ,  $C_3^r$  from the leptonic-channel cross section and the asymmetries  $A(\Delta\eta(\bar{b}, \ell))$  and  $A(\Delta\varphi(\bar{b}, \ell))$  with (a)  $\varepsilon_{\text{exp}} = 6\%$  and (b)  $\varepsilon_{\text{exp}} = 3\%$ . In each panel the lighter-gray region corresponds to  $\mathcal{P}_e = 0$ , the medium-gray region to  $\mathcal{P}_e = 0.4$  and the darker-gray region to  $\mathcal{P}_e = 0.7$ .

the initial-state  $\bar{b}$  and thus also the total four momentum of the process, which permits us to boost the event to other frames such as the partonic center-of-mass frame, or the  $\bar{t}$  rest frame. We can therefore obtain asymmetries for a large variety of kinematic observables, and look for the ones most sensitive to the anomalous couplings. In all cases, we compute the required cross sections with the cuts  $H_4$  as defined in (14).

The sensitivity to contact interactions entering only through decay vertices is negligible [35], as is clearly illustrated by the case of couplings involving muons in the leptonic channel discussed in



section V A. For that reason, in the hadronic channel we ignore diagrams (d), (f), (h) in Figure 5. On the other hand, we do retain in our computations the contribution of anomalous  $tbW$  couplings to the top decay vertex, which yields a non-negligible enhancement of the sensitivity to those couplings. Thus, the tree-level cross section we compute is quadratic in  $C_{1,\dots,4}$  and quartic in  $V_{L,R}, g_{L,R}$ . Within the ranges for the anomalous couplings determined by the bounds we obtain below, however, the contribution of the terms cubic and quartic in the anomalous  $tbW$  couplings is small. Thus, within those ranges, the cross section can be well approximated by a quadratic parameterization of the form (17), with  $(1 + \delta V_L)^4 \simeq 1 + 4\delta V_L + 6\delta V_L^2$ . The coefficients in (17) for the hadronic-channel unpolarized cross section, and for the polarized one with  $\mathcal{P}_e = +0.4$  and  $+0.7$ , are given in Appendix A. As noted in section V A, since (17) does not include interference terms involving two different effective couplings, it is appropriate only for obtaining bounds on the anomalous couplings taken one at a time. Nevertheless, we do take those missing interference terms into account in the computation of exclusion regions for pairs of effective couplings.

In Table XIV we report the bounds on the effective couplings obtained from the unpolarized cross section at the level of one standard deviation, assuming experimental errors of 7% and 12% as discussed in section IV B. As discussed in relation to Table X for the leptonic channel, the bounds on effective  $tbW$  couplings are almost independent of  $E_e$ , and those on contact-interaction couplings show a mild dependence on  $E_e$  that makes them somewhat tighter at higher energies. Also as in the case of the leptonic channel, the bounds on the imaginary parts  $C_{2,3,4}^i$  are the same as those on the real parts  $C_{2,3,4}^r$ . The bounds from the hadronic cross section shown in Table XIV are weaker than those in Table X from the leptonic channel, not surprisingly, since the assumed experimental errors in the former channel are about twice as large as those in the latter one.

In the hadronic channel some asymmetries yield significantly better sensitivity than the cross section, unlike what happens in the leptonic case. In Table XV we show bounds on the effective couplings obtained from the asymmetries indicated there, that are better than those from the cross section at the three energies  $E_e = 60, 140, 300$  GeV. The asymmetry  $A(\Delta\varphi(j_2, \cancel{E}_T), \pi/2)$  gives more restrictive bounds on  $V_R^r, V_R^i, g_R^r$  than  $\sigma$  (see Table XIV) at  $E_e = 60$  GeV, but not at 140 and 300 GeV, and for that reason they are not shown in Table XV. On the other hand, the bounds given by this asymmetry for  $g_R^i$  are slightly better than those from  $\sigma$ , as seen in the table. Similarly, the asymmetry  $A(\Delta\varphi(W^-, \cancel{E}_T), \pi/2)$  gives more restrictive bounds on  $C_{3,4}^{r,i}$ , than  $\sigma$  at  $E_e = 60$  GeV, but not at 140 and 300 GeV.

Notice that, as seen from Tables XV and X, the bounds on  $g_R^r, g_R^i$  obtained from  $\Delta\eta(\bar{b}, j_1)$  with  $\epsilon_{\text{exp}} = 7\%$  are actually tighter than those obtained from the leptonic cross section with  $\epsilon_{\text{exp}} = 3\%$ .

	$\epsilon_{\text{exp}} = 7\%$			$\epsilon_{\text{exp}} = 12\%$		
	60 GeV	140 GeV	300 GeV	60 GeV	140 GeV	300 GeV
$\delta V_L \times 10^2$	-1.79 1.70	-1.80 1.71	-1.80 1.71	-3.15 2.87	-3.15 2.88	-3.15 2.88
$V_R^r \times 10$	-1.49 1.77	-1.53 1.82	-1.55 1.83	-1.98 2.26	-2.04 2.32	-2.05 2.35
$V_R^i \times 10$	-1.63 1.63	-1.67 1.67	-1.69 1.69	-2.12 2.12	-2.17 2.17	-2.20 2.20
$g_R^r \times 10$	-0.54 0.62	-0.50 0.59	-0.48 0.57	-0.88 1.12	-0.82 1.07	-0.78 1.05
$g_R^i \times 10$	-1.61 1.61	-1.54 1.54	-1.48 1.48	-2.10 2.10	-2.01 2.01	-1.93 1.93
$g_L^r \times 10$	-1.30 1.07	-1.36 1.12	-1.36 1.14	-1.66 1.43	-1.72 1.49	-1.74 1.52
$g_L^i \times 10$	-1.18 1.18	-1.23 1.23	-1.24 1.24	-1.54 1.54	-1.60 1.60	-1.62 1.62
$C_1$	-0.48 0.51	-0.45 0.48	-0.43 0.46	-0.81 0.89	-0.76 0.85	-0.72 0.82
$C_2^{r,i}$	-5.31 5.31	-5.06 5.06	-4.62 4.62	-6.95 6.95	-6.62 6.62	-6.05 6.05
$C_3^{r,i}$	-3.29 3.29	-2.97 2.97	-2.65 2.65	-4.31 4.31	-3.88 3.88	-3.47 3.47
$C_4^{r,i}$	-5.14 5.14	-4.88 4.88	-4.45 4.45	-6.73 6.73	-6.39 6.39	-5.83 5.83

TABLE XIV: Bounds on effective couplings at the 68% CL obtained from the hadronic-channel unpolarized cross section by varying the couplings one at a time. The assumed experimental errors are 7% and 12%.

The bounds on  $C_2^{r,i}$  from those observables are essentially the same, despite the larger error in the hadronic channel. Similarly, the bounds on  $C_3^{r,i}$ ,  $C_4^{r,i}$  obtained from  $\Delta\varphi(j_2, \cancel{E}_T)$  with  $\epsilon_{\text{exp}} = 7\%$  are tighter than those obtained from the leptonic cross section with  $\epsilon_{\text{exp}} = 3\%$ . Furthermore, the bounds from hadronic asymmetries with  $\epsilon_{\text{exp}} = 7\%$  in Table XV are seen to be comparable to those from leptonic asymmetries with  $\epsilon_{\text{exp}} = 3\%$  in Table XII. In particular, the best hadronic-channel bounds on  $g_R^r$  with  $\epsilon_{\text{exp}} = 7\%$  are those from  $\Delta\eta(\bar{b}, j_1)$ , which are better than the best leptonic-channel bounds with  $\epsilon_{\text{exp}} = 3\%$  coming from  $\Delta\eta(\bar{b}, \ell)$ , at the three energies. Likewise, the best hadronic-channel bound on  $C_3^{r,i}$  obtained from  $\Delta\varphi(j_2, \cancel{E}_T)$  at  $E_e = 60$  GeV and  $\epsilon_{\text{exp}} = 7\%$  is better than the best leptonic-channel bound from  $\Delta\varphi(\bar{b}, \ell)$  at that energy with  $\epsilon_{\text{exp}} = 3\%$ .

For the contact-interaction couplings  $C_{2,3,4}^{r,i}$  involving right-handed electrons, the sensitivity can be significantly improved if the electron beam is right polarized. In Table XVI we give the bounds obtained for those couplings from the cross section by assuming initial-electron polarizations  $\mathcal{P}_e = +0.4$  and  $+0.7$ . Those bounds are tighter than the ones from the unpolarized cross section in Table XIV. At  $\mathcal{P}_e = +0.4$  they are comparable to, and at  $+0.7$  better than, the bounds from the unpolarized hadronic asymmetries in Table XV and from the unpolarized leptonic cross section, Table X, and unpolarized leptonic asymmetries, Table XII. On the other hand, the bounds from Table XVI are weaker than those from the leptonic-channel polarized cross section in Table XI.

As happens in the unpolarized case, with a right-polarized electron beam the sensitivity of

		$\epsilon_{\text{exp}} = 7\%$			$\epsilon_{\text{exp}} = 12\%$		
Observable		60 GeV	140 GeV	300 GeV	60 GeV	140 GeV	300 GeV
$V_R^r \times 10$	$\Delta\eta(\bar{b}, j_1)$	-1.21 1.31	-1.22 1.36	-1.20 1.37	-1.62 1.72	-1.64 1.78	-1.62 1.79
	$\Delta y(\bar{t}, \bar{b})$	-1.29 1.49	-1.26 1.39	-1.27 1.41	-1.76 1.93	-1.70 1.83	-1.71 1.84
	$\Delta y(\bar{t}, j_2)$	-1.32 1.44	-1.31 1.36	-1.27 1.37	-1.78 1.88	-1.75 1.79	-1.71 1.80
	$\Delta\eta(\bar{b}, j_2)$	-1.35 1.44	-1.30 1.35	-1.27 1.38	-1.81 1.90	-1.73 1.79	-1.70 1.81
$V_R^i \times 10$	$\Delta\eta(\bar{b}, j_1)$	-1.28 1.28	-1.29 1.29	-1.30 1.30	-1.70 1.70	-1.72 1.72	-1.72 1.72
	$\Delta y(\bar{t}, \bar{b})$	-1.37 1.37	-1.32 1.32	-1.32 1.32	-1.82 1.82	-1.76 1.76	-1.75 1.75
	$\Delta y(\bar{t}, j_2)$	-1.38 1.38	-1.31 1.31	-1.31 1.31	-1.83 1.83	-1.74 1.74	-1.73 1.73
	$\Delta\eta(\bar{b}, j_2)$	-1.38 1.38	-1.32 1.32	-1.32 1.32	-1.83 1.83	-1.75 1.75	-1.75 1.75
	$\Delta\eta(j_1, j_2)$	-1.59 1.59	-1.45 1.45	-1.36 1.36	-2.12 2.12	-1.93 1.93	-1.81 1.81
$g_R^r \times 10$	$\Delta\eta(\bar{b}, j_1)$	-0.18 0.18	-0.18 0.18	-0.17 0.17	-0.32 0.31	-0.31 0.30	-0.30 0.29
	$\Delta y(\bar{t}, \bar{b})$	-0.25 0.25	-0.21 0.21	-0.20 0.20	-0.43 0.43	-0.37 0.37	-0.34 0.34
	$\Delta\eta(\bar{b}, j_2)$	-0.35 0.36	-0.30 0.30	-0.27 0.27	-0.60 0.63	-0.50 0.51	-0.46 0.47
	$\Delta y(\bar{t}, j_2)$	-0.55 0.63	-0.45 0.50	-0.39 0.45	-0.90 1.22	-0.74 0.92	-0.66 0.81
$g_R^i \times 10$	$\Delta\eta(\bar{b}, j_1)$	-1.05 1.05	-1.02 1.02	-1.00 1.00	-1.39 1.39	-1.36 1.36	-1.32 1.32
	$\Delta y(\bar{t}, \bar{b})$	-1.19 1.19	-1.09 1.09	-1.05 1.05	-1.58 1.58	-1.45 1.45	-1.39 1.39
	$\Delta\eta(\bar{b}, j_2)$	-1.32 1.32	-1.20 1.20	-1.14 1.14	-1.76 1.76	-1.60 1.60	-1.52 1.52
	$\Delta\varphi(j_2, \cancel{E}_T)$	-1.35 1.35	-1.28 1.28	-1.23 1.23	-1.78 1.78	-1.70 1.70	-1.63 1.63
	$\Delta y(\bar{t}, j_2)$	-1.55 1.55	-1.39 1.39	-1.32 1.32	-2.08 2.08	-1.85 1.85	-1.76 1.76

TABLE XV: Bounds on effective couplings at the 68% CL obtained from the indicated hadronic-channel unpolarized asymmetries by varying the couplings one at a time. The definition of the asymmetries is analogous to that in table XII;  $j_1$  (resp.  $j_2$ ) refers to the light non- $b$  jet with the larger (resp. smaller)  $|\vec{p}_T|$ . The assumed experimental errors are 7% and 12%. (Continued on next page.)

some asymmetries is significantly better than that of the polarized cross section. In Table XVII we summarize the best bounds on  $C_{2,3,4}^{r,i}$  for the relevant asymmetries indicated there, for initial-electron polarizations  $\mathcal{P}_e = +0.4$  and  $+0.7$ . We omit for brevity the bounds on  $C_2^{r,i}$  obtained from the asymmetries of  $\Delta y(\bar{t}, j_2)$ ,  $\Delta y(\bar{t}, \bar{b})$ , which are essentially the same as those from  $\Delta\eta(\bar{b}, j_2)$ , as is the case also for the unpolarized asymmetries in Table XV. Due to the polarization, the bounds in that table are significantly better than those from the unpolarized asymmetries, Table XV, and due to the enhanced sensitivity of the asymmetries, also significantly better than the bounds from the polarized hadronic cross section, Table XVII. Furthermore, the bounds on  $C_{2,3,4}^{r,i}$  from polarized hadronic asymmetries in Table XVII are tighter than those from the unpolarized leptonic asymmetries in Table XII, most of them are better than those coming from the polarized leptonic

		$\epsilon_{\text{exp}} = 7\%$			$\epsilon_{\text{exp}} = 12\%$		
Observable		60 GeV	140 GeV	300 GeV	60 GeV	140 GeV	300 GeV
$C_2^{r,i}$	$\Delta\eta(\bar{b}, j_1)$	-3.75 3.75	-3.74 3.74	-3.51 3.51	-4.98 4.98	-4.96 4.96	-4.66 4.66
	$\Delta y(\bar{t}, \bar{b})$	-4.01 4.01	-3.84 3.84	-3.54 3.54	-5.33 5.33	-5.10 5.10	-4.71 4.71
	$\Delta y(\bar{t}, j_2)$	-4.03 4.03	-3.85 3.85	-3.59 3.59	-5.36 5.36	-5.12 5.12	-4.77 4.77
	$\Delta\eta(\bar{b}, j_2)$	-4.04 4.04	-3.85 3.85	-3.58 3.58	-5.36 5.36	-5.11 5.11	-4.77 4.77
	$\Delta\eta(j_1, j_2)$	-4.35 4.35	-3.97 3.97	-3.58 3.58	-5.79 5.79	-5.27 5.27	-4.77 4.77
$C_3^{r,i}$	$\Delta\varphi(j_2, \cancel{E}_T)$	-2.16 2.16	-1.85 1.85	-1.61 1.61	-2.85 2.85	-2.44 2.44	-2.13 2.13
	$\Delta\varphi(j_1, j_2)$	-2.51 2.51	-1.88 1.88	-1.50 1.50	-3.33 3.33	-2.49 2.49	-1.97 1.97
$C_4^{r,i}$	$\Delta\varphi(j_2, \cancel{E}_T)$	-3.70 3.70	-3.25 3.25	-2.82 2.82	-4.91 4.91	-4.31 4.31	-3.74 3.74
	$\Delta\varphi(j_1, j_2)$	-4.28 4.28	-3.30 3.30	-2.63 2.63	-5.70 5.70	-4.37 4.37	-3.47 3.47

TABLE XV: (Continued from previous page.)

		$\epsilon_{\text{exp}} = 7\%$			$\epsilon_{\text{exp}} = 12\%$		
		60 GeV	140 GeV	300 GeV	60 GeV	140 GeV	300 GeV
$\mathcal{P}_e = 0.4$	$C_2^{r,i}$	$\pm 3.47$	$\pm 3.31$	$\pm 3.03$	$\pm 4.55$	$\pm 4.33$	$\pm 3.97$
	$C_3^{r,i}$	$\pm 2.16$	$\pm 1.95$	$\pm 1.74$	$\pm 2.83$	$\pm 2.55$	$\pm 2.27$
	$C_4^{r,i}$	$\pm 3.37$	$\pm 3.20$	$\pm 2.92$	$\pm 4.41$	$\pm 4.19$	$\pm 3.82$
$\mathcal{P}_e = 0.7$	$C_2^{r,i}$	$\pm 2.23$	$\pm 2.12$	$\pm 1.94$	$\pm 2.92$	$\pm 2.78$	$\pm 2.54$
	$C_3^{r,i}$	$\pm 1.39$	$\pm 1.25$	$\pm 1.11$	$\pm 1.81$	$\pm 1.63$	$\pm 1.46$
	$C_4^{r,i}$	$\pm 2.16$	$\pm 2.05$	$\pm 1.87$	$\pm 2.83$	$\pm 2.69$	$\pm 2.45$

TABLE XVI: Bounds at the 68% CL on contact-interaction couplings involving initial right-polarized electrons, obtained from the hadronic-channel polarized cross section by varying the couplings one at a time. The assumed experimental errors are 7% and 12%. The asymmetries of  $\Delta y(\bar{t}, j_2)$  and  $\Delta y(\bar{t}, \bar{b})$  yield the same bounds on  $C_2^{r,i}$  as  $\Delta\eta(\bar{b}, j_2)$ .

cross section in Table XI, and they are only slightly weaker than the bounds from polarized leptonic asymmetries, Table XIII, despite the fact that the experimental errors assumed in the hadronic channel are twice as large as those in the leptonic channel.

The asymmetries discussed so far are all based on longitudinal-boost invariant kinematic observables measured in the lab frame not involving longitudinal neutrino momenta. We have considered several other asymmetries of the same type, that we briefly mention here. We have not included in tables XIV–XVII the bounds obtained from the asymmetry  $A(\Delta y(\bar{t}, j_1))$ . At  $E_e = 60$  GeV this asymmetry gives the best bounds we have found for  $C_2^{r,i}$ ,  $V_R^{r,i}$ ,  $g_R^{r,i}$ ,  $g_L^{r,i}$ . At  $E_e = 140, 300$  GeV, however, the bounds from this asymmetry are significantly less tight. This phenomenon suggests

		Observable	$\epsilon_{\text{exp}} = 7\%$			$\epsilon_{\text{exp}} = 12\%$		
			60 GeV	140 GeV	300 GeV	60 GeV	140 GeV	300 GeV
$\mathcal{P}_e = 0.4$	$C_2^{r,i}$	$\Delta\eta(\bar{b}, j_1)$	$\pm 2.47$	$\pm 2.43$	$\pm 2.29$	$\pm 3.27$	$\pm 3.23$	$\pm 3.05$
		$\Delta\eta(\bar{b}, j_2)$	$\pm 2.64$	$\pm 2.52$	$\pm 2.35$	$\pm 3.50$	$\pm 3.35$	$\pm 3.13$
		$\Delta\eta(j_1, j_2)$	$\pm 2.83$	$\pm 2.59$	$\pm 2.33$	$\pm 3.76$	$\pm 3.45$	$\pm 3.09$
	$C_3^{r,i}$	$\Delta\varphi(j_2, \cancel{E}_T)$	$\pm 1.42$	$\pm 1.21$	$\pm 1.05$	$\pm 1.88$	$\pm 1.60$	$\pm 1.39$
		$\Delta\varphi(j_1, j_2)$	$\pm 1.64$	$\pm 1.23$	$\pm 0.98$	$\pm 2.18$	$\pm 1.63$	$\pm 1.29$
	$C_4^{r,i}$	$\Delta\varphi(j_2, \cancel{E}_T)$	$\pm 2.46$	$\pm 2.13$	$\pm 1.86$	$\pm 3.26$	$\pm 2.82$	$\pm 2.45$
$\Delta\varphi(j_1, j_2)$		$\pm 2.81$	$\pm 2.16$	$\pm 1.72$	$\pm 3.74$	$\pm 2.86$	$\pm 2.27$	
$\mathcal{P}_e = 0.7$	$C_2^{r,i}$	$\Delta\eta(\bar{b}, j_1)$	$\pm 1.58$	$\pm 1.57$	$\pm 1.47$	$\pm 2.09$	$\pm 2.08$	$\pm 1.95$
		$\Delta\eta(\bar{b}, j_2)$	$\pm 1.69$	$\pm 1.62$	$\pm 1.51$	$\pm 2.25$	$\pm 2.16$	$\pm 2.01$
		$\Delta\eta(j_1, j_2)$	$\pm 1.81$	$\pm 1.66$	$\pm 1.49$	$\pm 2.41$	$\pm 2.21$	$\pm 1.99$
	$C_3^{r,i}$	$\Delta\varphi(j_2, \cancel{E}_T)$	$\pm 0.91$	$\pm 0.78$	$\pm 0.68$	$\pm 1.20$	$\pm 1.03$	$\pm 0.89$
		$\Delta\varphi(j_1, j_2)$	$\pm 1.05$	$\pm 0.79$	$\pm 0.63$	$\pm 1.40$	$\pm 1.04$	$\pm 0.83$
	$C_4^{r,i}$	$\Delta\varphi(j_2, \cancel{E}_T)$	$\pm 1.57$	$\pm 1.37$	$\pm 1.19$	$\pm 2.08$	$\pm 1.81$	$\pm 1.57$
		$\Delta\varphi(j_1, j_2)$	$\pm 1.80$	$\pm 1.39$	$\pm 1.10$	$\pm 2.40$	$\pm 1.84$	$\pm 1.46$

TABLE XVII: Bounds at the 68% CL on contact-interaction couplings involving initial right-handed electrons, obtained from the indicated hadronic-channel asymmetries by varying the couplings one at a time. The definition of the asymmetries is as in table XII. The assumed experimental errors are 7% and 12%.

that those bounds may not be fully reliable, as is discussed in more detail in Appendix B. The asymmetries of  $\Delta y(\bar{t}, W)$  and  $\Delta y(\bar{b}, W)$  yield bounds on the effective couplings that are the same as, or weaker than, those from  $\Delta y(\bar{t}, \bar{b})$  given in the tables. The asymmetries  $\Delta y(j_{1,2}, W)$  give the same bounds as  $\Delta\eta(j_1, j_2)$ , and the asymmetry  $A(\Delta\varphi(j_1, W), \pi/2) \equiv 1$ . The asymmetries of  $\Delta\varphi(\bar{b}, j_{1,2})$ ,  $\Delta\varphi(\bar{b}, W)$ ,  $\Delta\varphi(j_2, W)$ ,  $\Delta\varphi(\bar{b}, \cancel{E}_T)$ ,  $\Delta\varphi(j_1, \cancel{E}_T)$ , all give bounds on the effective couplings that are weaker than those from the cross section and therefore not worth examining in detail.

We have also considered the asymmetries associated with the lab frame observables  $\cos(\bar{t}, j_{1,2})$ ,  $\cos(\bar{t}, W)$ ,  $\cos(\bar{t}, \bar{b})$ ,  $\cos(\bar{b}, j_{1,2})$ ,  $\cos(\bar{b}, W)$ ,  $\cos(j_{1,2}, W)$ ,  $\cos(j_1, j_2)$ . We have not found any significant sensitivity to the anomalous couplings for any of them.

Another class of lab-frame kinematic observables giving rise to asymmetries involves the reconstructed longitudinal momentum of the final-state neutrino. Notice that to measure experimentally the asymmetries of these observables a full reconstruction of the hard-event kinematics is needed, which can give rise to systematic errors additional to those involved in pure lab frame measurements. For the purpose of obtaining bounds at the one-sigma level, we nevertheless assume the

same experimental errors as in the case of lab frame observables in order to compare the sensitivities of the two classes of observables. Within this class we have considered the longitudinal-boost invariants  $\Delta\eta(x, \nu_e)$  with  $x = j_{1,2}, \bar{b}, \Delta y(\bar{t}, \nu_e)$  and  $\Delta y(W, \nu_e)$ . Notice that the asymmetry  $A(\Delta y(\bar{t}, \nu_e))$  is equal to the asymmetry of the longitudinal momentum of  $\bar{t}$  in the center of mass frame,  $A(p_z(\bar{t})_{c.m.})$ . These five asymmetries possess poor sensitivity to anomalous  $tbW$  couplings, but they are sensitive to the contact-interaction couplings  $C_{2,3,4}^{r,i}$  for which all of them give similar results, better than those from  $\sigma$  in Table XIV. On the other hand, the best bounds for  $C_{2,3,4}^{r,i}$  given in Table XV are better than those obtained from these asymmetries, and for this reason we did not include them in that table.

Another class of asymmetries is based on the observables  $\cos(\bar{t}_{c.m.}, x_{c.m.})$  with  $x = j_{1,2}, \bar{b}, W$ . Since both momenta are measured in the center-of-mass frame, these observables also require full reconstruction of the event kinematics. We do not find significant sensitivity to any of the anomalous couplings in these asymmetries.

We have also studied the class of observables of the form  $\cos(\bar{t}_{c.m.}, x_*)$ ,  $x = j_1, j_2, \bar{b}, W$ , where  $\bar{t}_{c.m.}$  refers to the momentum of  $\bar{t}$  in the c.m. frame and  $x_*$  to the momentum of  $x$  in the rest frame of  $\bar{t}$ . This class of observables has been considered in the literature in connection with top quark polarization [57]. They obviously require a full reconstruction of the partonic kinematics so, as mentioned above, they may be affected by systematical errors beyond those involved in pure lab frame measurements. The asymmetries  $A(\cos(\bar{t}_{c.m.}, x_*))$  are found to have good sensitivity to  $C_{3,4}^{r,i}$  and  $V_R^{r,i}$ , and to a lesser extent to  $C_2^{r,i}$ . The most sensitive to these anomalous couplings is  $\cos(\bar{t}_{c.m.}, j_{1*})$ , which yields bounds that are tighter than those from lab-frame asymmetries in Table XV. A summary of the results obtained from this asymmetry is given in Table XVIII. The asymmetries  $\cos(\bar{t}_{c.m.}, W_*)$  and  $\cos(\bar{t}_{c.m.}, \bar{b}_*)$  also have good sensitivity, leading to bounds that are weaker than the tightest ones in Table XV, but stricter than those from the cross section in Table XIV. The asymmetry  $\cos(\bar{t}_{c.m.}, j_{2*})$  does not yield better bounds than  $\sigma$ .

Finally, the single-coupling bounds obtained from a further class of observables not considered here is briefly discussed at the end of Appendix B.

We now turn to correlated regions of allowed parameter space, obtained by considering two effective couplings to be simultaneously non-vanishing and by supplying the necessary additional interference terms in (17). Figure 11 shows the allowed regions at the 68% confidence level (CL) and at  $E_e = 60$  GeV, assuming an unpolarized electron beam in all cases, for  $\delta V_L$  versus  $V_R^r$ ,  $g_R^r$ ,  $g_L^r$  and  $C_1$ . Figures 11 (a) and (b) show the allowed regions for  $V_R^r$  and  $g_R^r$ , respectively, as determined by the level curves of the cross section and  $A(\Delta\eta(\bar{b}, j_1))$ . As seen in the figure, those

		$\epsilon_{\text{exp}} = 7\%$			$\epsilon_{\text{exp}} = 12\%$		
		60 GeV	140 GeV	300 GeV	60 GeV	140 GeV	300 GeV
$\mathcal{P}_e = 0.0$	$V_R^r \times 10$	-0.87 0.96	-0.63 0.74	-0.47 0.51	-1.16 1.25	-0.85 0.95	-0.62 0.66
	$V_R^i \times 10$	$\pm 0.90$	$\pm 0.67$	$\pm 0.49$	$\pm 1.18$	$\pm 0.88$	$\pm 0.65$
	$C_2^{r,i}$	$\pm 4.16$	$\pm 2.39$	$\pm 1.48$	$\pm 5.53$	$\pm 3.14$	$\pm 1.94$
	$C_3^{r,i}$	$\pm 1.36$	$\pm 0.83$	$\pm 0.54$	$\pm 1.79$	$\pm 1.09$	$\pm 0.71$
	$C_4^{r,i}$	$\pm 2.32$	$\pm 1.46$	$\pm 0.95$	$\pm 3.05$	$\pm 1.91$	$\pm 1.24$
$\mathcal{P}_e = 0.4$	$C_2^{r,i}$	$\pm 2.71$	$\pm 1.53$	$\pm 0.96$	$\pm 3.60$	$\pm 2.02$	$\pm 1.26$
	$C_3^{r,i}$	$\pm 0.89$	$\pm 0.54$	$\pm 0.35$	$\pm 1.17$	$\pm 0.71$	$\pm 0.46$
	$C_4^{r,i}$	$\pm 1.51$	$\pm 0.94$	$\pm 0.62$	$\pm 1.99$	$\pm 1.24$	$\pm 0.81$
$\mathcal{P}_e = 0.7$	$C_2^{r,i}$	$\pm 1.73$	$\pm 0.99$	$\pm 0.62$	$\pm 2.30$	$\pm 1.30$	$\pm 0.81$
	$C_3^{r,i}$	$\pm 0.57$	$\pm 0.35$	$\pm 0.23$	$\pm 0.75$	$\pm 0.46$	$\pm 0.30$
	$C_4^{r,i}$	$\pm 0.97$	$\pm 0.61$	$\pm 0.40$	$\pm 1.28$	$\pm 0.80$	$\pm 0.52$

TABLE XVIII: Bounds on effective couplings at the 68% CL obtained by varying the couplings one at a time in the asymmetry  $A(\cos(\bar{t}_{\text{c.m.}}, j_{1*}))$ , with  $j_1$  the light non- $b$  jet with the larger  $|\vec{p}_T|$ . The assumed experimental errors are 7% and 12%.

observables yield closed regions consistent with the bounds given in tables XIV and XV. In the case of  $\delta V_L$  .vs.  $g_L^r$  the only observable with significant sensitivity is the cross section, which gives an elliptical corona containing the origin at its periapsis as allowed region. In order to restrict that region to a neighborhood of the origin we use the asymmetry  $A(\Delta\varphi(j_2, \cancel{E}_T))$  which has a somewhat poor sensitivity to  $g_L^r$ , as shown in Figure 11 (c). As a result, the bounds on  $g_L^r$  displayed in the figure are less restrictive than those in Table XIV. For  $C_1$  and  $\delta V_L$  the cross section is the only available observable with any sensitivity which, as seen in Figure 11 (d), for small values of those couplings depends on them only through the linear combination  $\simeq \delta V_L + (5/4)v^2/(2\Lambda^2)C_1$ . As in Figure 6 for the leptonic channel, we include in Figure 11 (d), for reference, the current bounds  $V_L = 0.998 \pm 0.038$  (exp) from CMS [30].

We have also considered the allowed regions on the complex plane of the  $tbW$  couplings  $V_R$ ,  $g_R$  and  $g_L$ . For  $V_R$ , the allowed region is obtained from the asymmetry  $A(\Delta(\eta(\bar{b}, j_1)))$  which gives the best bounds on that coupling. It consists of a solid ellipse inscribed in the rectangle formed with the single-coupling bounds in Table XV. Similarly, the best bounds for  $g_L$  are obtained from the unpolarized cross section, which leads to an allowed region in the  $g_L^r - g_L^i$  plane consisting of a solid ellipse inscribed in the rectangle formed by the bounds in Table XIV. A figure is clearly not needed for these ellipses. The best bounds on  $g_R$  are obtained from  $A(\Delta\eta(\bar{b}, j_1))$ , which determines an

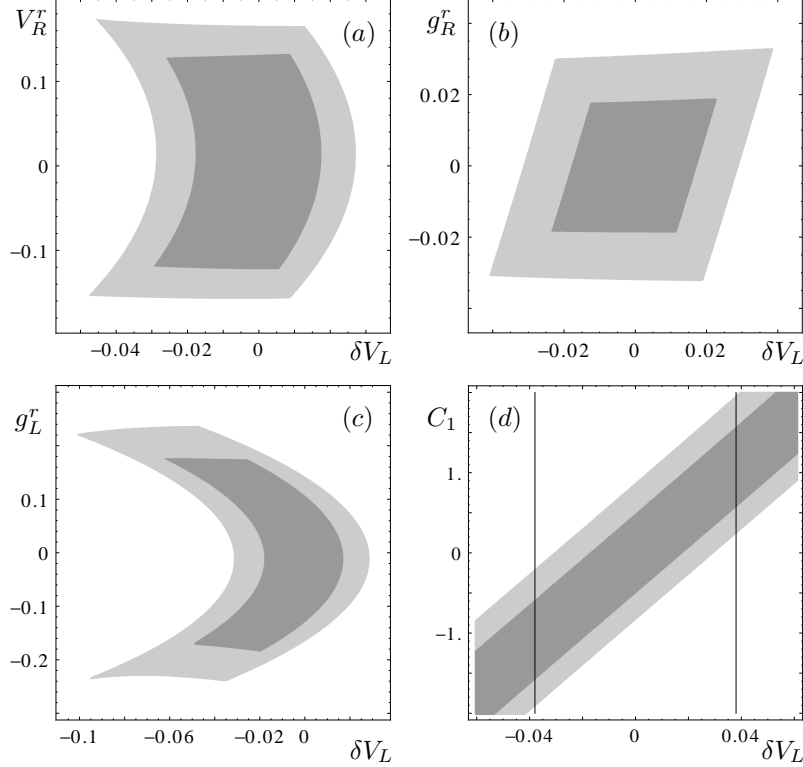


FIG. 11: Allowed regions at 68% CL at  $E_e = 60$  GeV for (a)  $\delta V_L$ ,  $V_R$  from the cross section and the asymmetry  $A(\Delta\eta(\bar{b}, j_1))$ , (b)  $\delta V_L$ ,  $g_R$  from the cross section and the asymmetry  $A(\Delta\eta(\bar{b}, j_1))$ , (c)  $\delta V_L$ ,  $g_L$  from the cross section and the asymmetry  $A(\Delta\varphi(j_2, \cancel{E}_T))$ , (d)  $\delta V_L$ ,  $C_1$  from the cross section. The vertical lines in (d) correspond to the current bounds  $|\delta V_L| < 0.038$  [30]. The light-gray regions correspond to  $\varepsilon_{\text{exp}} = 12\%$ , the darker regions to  $\varepsilon_{\text{exp}} = 7\%$ .

allowed region shaped as a two-dimensional toroidal region containing the origin. The asymmetry  $A(\Delta(\varphi(j_2, \cancel{E}_T)))$  has some sensitivity to  $g_R^i$  and the allowed region it determines cleanly intersects the previous toroid. The allowed region in the complex  $g_R$  plane at the 68% CL at  $E_e = 60$  GeV is shown in Figure 12 for both  $\varepsilon_{\text{exp}} = 12\%$  and  $\varepsilon_{\text{exp}} = 7\%$ .

The allowed regions for  $C_2^r - C_2^i$  (from  $A(\Delta(\eta(\bar{b}, j_1)))$ ) and for  $C_3^r - C_3^i$  and  $C_4^r - C_4^i$  (from  $A(\Delta(\varphi(j_2, / E_T)))$ ) are ellipses inscribed in the rectangle formed with the single-coupling bounds from tables XV and XVII. There is, then, no need to display them explicitly.

Figure 13 shows the allowed regions in the four planes  $g_L - g_R$ , determined by the cross section and the asymmetry  $A(\Delta\eta(\bar{b}, j_1))$  at 68% CL and  $E_e = 60$  GeV.

In Figure 14 we display the allowed regions for the contact–interaction couplings  $C_{2,3,4}^r$  versus  $C_1$ , determined by the unpolarized cross section, which bounds  $C_1$ , and the polarized asymmetries  $A(\Delta\eta(\bar{b}, j_1))$  (which bounds  $C_2^r$ ) and  $A(\Delta\varphi(j_2, \cancel{E}_T))$  (which bounds  $C_{3,4}^r$ ). The effect of polarization



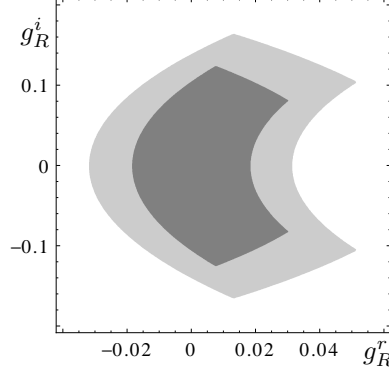


FIG. 12: Allowed regions at 68% CL at  $E_e = 60$  GeV for  $g_R$  obtained from the asymmetries  $A(\Delta\eta(\bar{b}, j_1))$  and  $A(\Delta\varphi(j_2, \cancel{E}_T))$ . The light-gray area corresponds to  $\varepsilon_{\text{exp}} = 12\%$ , the darker one to  $\varepsilon_{\text{exp}} = 7\%$ .

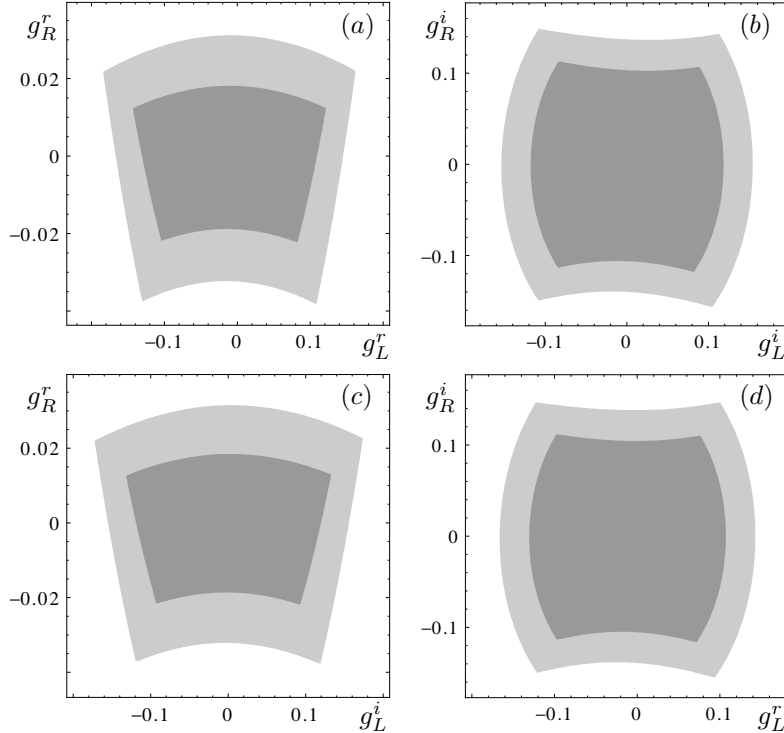


FIG. 13: Allowed regions at 68% CL at  $E_e = 60$  GeV, from the hadronic cross section and the asymmetry  $A(\Delta\eta(\bar{b}, j_1))$ , with  $\varepsilon_{\text{exp}} = 12\%$  (light gray) and  $\varepsilon_{\text{exp}} = 7\%$  (dark gray).

on the sensitivity of the asymmetries on  $C_{2,3,4}$  is clearly shown in the figure. Notice that the areas defined by each gray tone are (simply) connected, though they look disconnected in the figure because they are stacked on one another.

Figure 15 shows the allowed regions in the planes  $C_2^r - C_3^r$  (determined by the cross section and the asymmetries  $A(\Delta\eta(\bar{b}, j_1))$  and  $A(\Delta\varphi(j_2, \cancel{E}_T))$ ) and  $C_3^r - C_4^r$  (determined by the cross section and the asymmetry  $A(\Delta\varphi(j_2, \cancel{E}_T))$ ), at 68% CL and  $E_e = 60$  GeV, for  $\varepsilon_{\text{exp}} = 7\%$  and 12%, and for

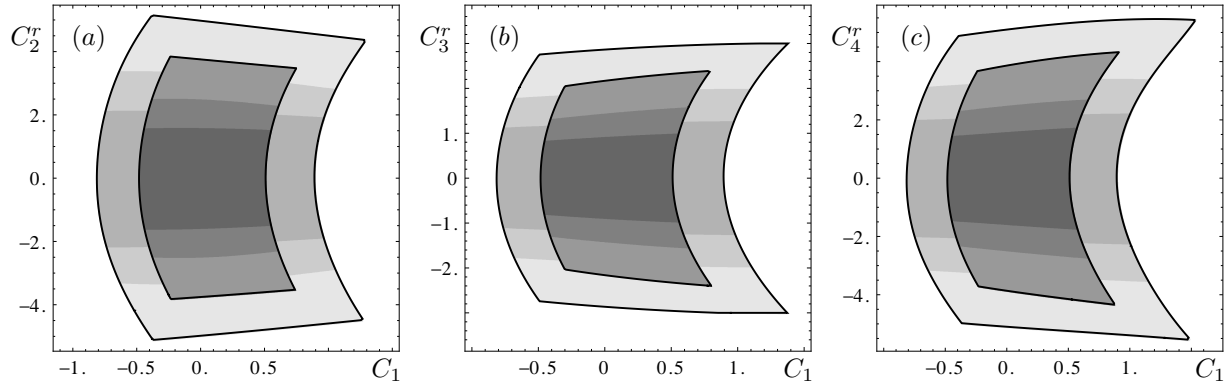


FIG. 14: Allowed regions at 68% CL at  $E_e = 60$  GeV for (a)  $C_1^r, C_2^r$  from the unpolarized cross section and the asymmetry  $A(\Delta\eta(\bar{b}, j_1))$ , (b)  $C_1^r, C_3^r$  from the unpolarized cross section and the asymmetry  $A(\Delta\varphi(j_2, \cancel{E}_T))$ , (c)  $C_1^r, C_4^r$  from the unpolarized cross section and the asymmetry  $A(\Delta\varphi(j_2, \cancel{E}_T))$ . The larger quadrangles in each panel correspond to  $\varepsilon_{\text{exp}} = 12\%$ , the smaller ones to  $\varepsilon_{\text{exp}} = 7\%$ . Within each quadrangle the lighter-gray region corresponds to  $\mathcal{P}_e = 0$ , the medium-gray region to  $\mathcal{P}_e = 0.4$  and the darker-gray region to  $\mathcal{P}_e = 0.7$ .

the three polarizations  $\mathcal{P}_e = 0, +0.4, +0.7$ . Here the effect of the polarization on the sensitivity is apparent, and also the fact that the interference terms proportional to  $C_3^r C_4^r$  are significantly larger than those proportional to  $C_2^r C_3^r$ . The allowed regions in the planes of the imaginary parts  $C_2^i - C_3^i$  and  $C_3^i - C_4^i$  are identical to those in the figure for the real parts. Although the interference terms proportional to  $C_3^r C_4^i$  and  $C_3^i C_4^r$  do not vanish, they turn out to be small. As a result, the allowed regions in the planes  $C_3^r - C_4^i$  and  $C_3^i - C_4^r$  are solid ellipses inscribed in the rectangles determined by the bounds from  $A(\Delta\varphi(j_2, \cancel{E}_T))$  in tables XV and XVII.

## VI. CONCLUSIONS

In this paper we have investigated the sensitivity of the LHeC to probe new physics in single-antitop production within the framework of the most general  $SU(2)_L \times U(1)$ -gauge invariant effective Lagrangian of dimension six. In this theoretical context, a systematic study of single-antitop production must take into account the fact that the usual operator basis associated with the top-quark charged-current interaction Lagrangian (5) is complete only up to four-fermion operators [8, 13, 17]. The appropriate complete Lagrangian is discussed in Section II.

Since the LHeC will necessarily run simultaneously with the HL-LHC, it is of interest to try to estimate the potential sensitivity to the effective couplings of both programs. We do that in Section III, in a simplified approach involving  $W$  helicity fractions in top decay (in the approximation

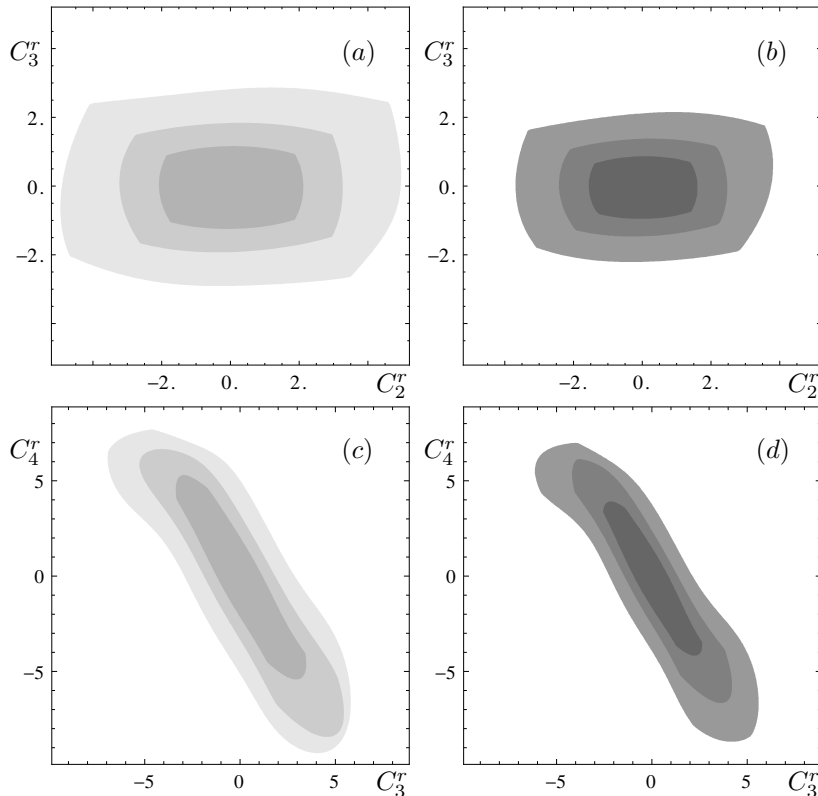


FIG. 15: Upper row: allowed regions at 68% CL at  $E_e = 60$  GeV for  $C_2^r$ ,  $C_3^r$  from the cross section and the asymmetries  $A(\Delta\eta(\bar{b}, j_1))$  and  $A(\Delta\varphi(j_2, \cancel{E}_T))$  with (a)  $\varepsilon_{\text{exp}} = 12\%$  and (b)  $\varepsilon_{\text{exp}} = 7\%$ . Lower row: allowed regions at 68% CL at  $E_e = 60$  GeV for  $C_3^r$ ,  $C_4^r$  from the cross section and the asymmetry  $A(\Delta\varphi(j_2, \cancel{E}_T))$  with (c)  $\varepsilon_{\text{exp}} = 12\%$  and (d)  $\varepsilon_{\text{exp}} = 7\%$ . In each panel the lighter-gray region corresponds to  $\mathcal{P}_e = 0$ , the medium-gray region to  $\mathcal{P}_e = 0.4$  and the darker-gray region to  $\mathcal{P}_e = 0.7$ .

$t \rightarrow bW$ ) at the LHC and single-top production (in the two-body approximation) at the LHC and LHeC, and taking input from recent experimental data from CMS. For simplicity, we consider only cross-section measurements and  $CP$ -even couplings. Our estimates indicate that the LHeC should significantly improve the bounds of the HL-LHC on  $V_L$ , and lead to somewhat tighter bounds on  $V_R$ . The tensor couplings  $g_{L,R}$  would be moderately better constrained by the HL-LHC than the LHeC. The bounds on the contact-interaction coupling  $C_1$  at the LHeC are expected from our estimates to be smaller than those on  $g_\times$  at the HL-LHC by a factor of 2.

In Section IV we considered single-top production in the Standard Model in both leptonic and hadronic channel. We found that backgrounds in leptonic channel are quite mild, leading to a lower bound on the experimental error as low as 3%. In the hadronic channel, on the other hand, a strong reducible background results in expected experimental uncertainties about twice as large as in the leptonic channel. For polarizations less than 90%, our error estimates are roughly independent of

electron beam polarization.

In Section V we obtained bounds from the cross section and several asymmetries on the eight effective couplings, for three values of the electron beam energy ( $E_e = 60, 140, 300$  GeV), three values of polarization ( $\mathcal{P}_e = 0, 40\%, 70\%$ ), and for the various values of experimental uncertainty assumed in the previous section. The cross section is the only observable we found to be significantly sensitive to the couplings  $V_L$ ,  $g_L$  and  $C_1$ . For them, the tightest bounds come from the leptonic channel cross section due to its small expected experimental error. In the leptonic channel, discussed in Section V A, there are only three asymmetries that give better sensitivity to some of the remaining couplings  $V_R$ ,  $g_R$ ,  $C_{2,3,4}$  than that of the cross section. These are the asymmetries of  $\Delta\eta(\bar{b}, \ell)$  (sensitive to  $C_2$ ,  $V_r$  and  $g_R$ ),  $\Delta\varphi(\bar{b}, \ell)$  (sensitive to  $C_{3,4}$ ) and  $\Delta\varphi(\ell, \cancel{E}_T)$  (sensitive to  $C_3$ ). The bounds obtained from these asymmetries, however, are only modestly tighter than the ones from the cross section. (With the only exception of  $C_2$ , for which the bounds resulting from the cross section are about twice as large as those from the asymmetry of  $\Delta\eta(\bar{b}, \ell)$ .)

The hadronic channel of single-top production is especially interesting because it has not been experimentally observed until now. The bounds obtained from the cross section in that channel are looser than those from the leptonic one because the errors assumed for the former are twice as large as those of the latter. In this channel, however, it is possible to completely determine the kinematics of the underlying partonic event, which gives rise to a large spectrum of measurable asymmetries. In section V B, we made an extensive survey of kinematic observables and assessed the sensitivity of their asymmetries to the anomalous couplings. Unlike the leptonic case, in the hadronic one several asymmetries were found to possess much higher sensitivity than the cross section. Those asymmetries yield bounds on some effective couplings that are almost as tight as the corresponding bounds in the leptonic channel with half the experimental error. In a few cases, the hadronic asymmetries yield even slightly better bounds than the leptonic ones. That is the case of the bounds on  $g_R^r$  from the asymmetry of  $\Delta\eta(\bar{b}, j_1)$ , and those on  $C_{3,4}^r$  from  $\Delta\varphi(j_2, \cancel{E}_T)$ . For the four-fermion couplings  $C_{2,3,4}$ , involving right-handed electrons, a right-polarized beam results in a strong sensitivity enhancement.

In summary, the LHeC will provide a clean experimental environment in which it will be possible to obtain bounds on the  $tbW$  vertex that will be competitive with those from the HL-LHC, and in the case of the vector form-factors arguably even better. Furthermore, the LHeC will provide unique information on four-fermion contact interactions involving third-generation quarks and first-generation leptons. Thus, the input from the LHeC will be very useful in studying the effective dimension six operators relevant to top-quark physics.

**Acknowledgments** We acknowledge support from Conacyt and Sistema Nacional de Investigadores de México.

- 
- [1] J. L. Abelleira Fernandez *et al.* [LHeC Study Group Collaboration], J. Phys. G **39**, 075001 (2012). See [arXiv:1206.2913v2 [physics.acc-ph]].
- [2] O. Bruening and M. Klein, Mod. Phys. Lett. A **28**, no. 16, 1330011 (2013).
- [3] H. Abramowicz *et al.* [ZEUS Collaboration], Phys. Rev. D **86**, 012005 (2012) [arXiv:1205.5179 [hep-ex]]; M. Sahin, S. Sultansoy and S. Turkoz, Phys. Lett. B **689**, 172 (2010) [arXiv:1001.4505 [hep-ph]]; J. M. Arnold, B. Fornal and M. B. Wise, Phys. Rev. D **88**, 035009 (2013) [arXiv:1304.6119 [hep-ph]].
- [4] L. Duarte, G. A. González-Sprinberg, O. A. Sampayo, Phys. Rev. D **91** (2015) 053007.
- [5] S. S. Biswal, R. M. Godbole, B. Mellado and S. Raychaudhuri, Phys. Rev. Lett. **109**, 261801 (2012).
- [6] T. Han and B. Mellado, Phys. Rev. D **82**, 016009 (2010); A. Senol, Nucl. Phys. B **873**, 293 (2013); W. Zhe, W. Shao-Ming, M. Wen-Gan, G. Lei and Z. Ren-You, Phys. Rev. D **83**, 055003 (2011); I. T. Cakir, O. Cakir, A. Senol and A. T. Tasci, Mod. Phys. Lett. A **28**, no. 31, 1350142 (2013).
- [7] U. Baur and D. Zeppenfeld, Nucl. Phys. B **325**, 253 (1989); U. Baur and M. A. Doncheski, Phys. Rev. D **46**, 1959 (1992); C. S. Kim and W. J. Stirling, Z. Phys. C **53**, 601 (1992); T. Helbig and H. Spiesberger, Nucl. Phys. B **373**, 73 (1992); S. Godfrey, Z. Phys. C **55**, 619 (1992); C. S. Kim, J. Lee and H. S. Song, Z. Phys. C **63**, 673 (1994); S. Atag and I. T. Cakir, Phys. Rev. D **63**, 033004 (2001); C. Brenner Mariotto and M. V. T. Machado, Phys. Rev. D **86**, 033009 (2012); S. S. Biswal, M. Patra and S. Raychaudhuri, arXiv:1405.6056 [hep-ph]; I. T. Cakir, O. Cakir, A. Senol and A. T. Tasci, Acta Phys. Polon. B **45**, 1947 (2014)
- [8] F. Bach and T. Ohl, Phys. Rev. D **86**, 114026 (2012).
- [9] S. Dutta, A. Goyal, M. Kumar and B. Mellado, arXiv:1307.1688 [hep-ph].
- [10] J. D. Wells, *Effective Theories in Physics: From Planetary Orbits to Elementary Particle Masses* (Springer, 2012), [arXiv:1211.0634 [physics.hist-ph]]; S. Weinberg, PoS CD **09**, 001 (2009), [arXiv:0908.1964 [hep-th]].
- [11] W. Buchmueller and D. Wyler, Nucl. Phys. B **268** (1986) 621.
- [12] B. Grzadkowski, Z. Hioki, K. Ohkuma, J. Wudka, Nucl. Phys. B **689**, 108 (2004).
- [13] J. A. Aguilar-Saavedra, Nucl. Phys. B **812** (2009) 181.
- [14] B. Grzadkowski, M. Iskrzynski, M. Misiak, J. Rosiek, JHEP **1010**, 085 (2010).
- [15] M. B. Einhorn and J. Wudka, Nucl. Phys. B **876**, 556 (2013).
- [16] J. A. Aguilar-Saavedra, Nucl. Phys. B **821** (2009) 215.
- [17] J. A. Aguilar-Saavedra, Nucl. Phys. B **843**, 638 (2011); [Erratum-ibid. B **851**, 443 (2011)].
- [18] Q. H. Cao, J. Wudka and C.-P. Yuan, Phys. Lett. B **658**, 50 (2007).
- [19] F. Bach and T. Ohl, Phys. Rev. D **90** (2014) 074022.

See also,

- J. Gao, C. S. Li and C. P. Yuan, JHEP **1207**, 037 (2012)
- [20] D. Duffty and Z. Sullivan, Phys. Rev. D **86**, 075018 (2012); N. Vignaroli, Phys. Rev. D **89**, 095027 (2014).
- [21] J. L. Hewett and T. G. Rizzo, Phys. Rev. D **56**, 5709 (1997); A. Belyaev, C. Leroy, R. Mehdiyev and A. Pukhov, JHEP **0509**, 005 (2005); O. J. P. Eboli, M. C. Gonzalez-Garcia and J. K. Mizukoshi, Phys. Lett. B **396**, 238 (1997).
- [22] J. Barranco, D. Delepine, V. Gonzalez Macias and L. Lopez-Lozano, arXiv:1404.0454 [hep-ph] S. Davidson and P. Verdier, Phys. Rev. D **83**, 115016 (2011); J. M. Arnold, B. Fornal and M. B. Wise, Phys. Rev. D **88**, 035009 (2013)
- [23] A. O. Bouzas and F. Larios, Phys. Rev. D **88**, 094007 (2013).
- [24] C. Zhang, N. Greiner, S. Willenbrock, Phys. Rev. D **86**, 014024 (2012).
- [25] A. O. Bouzas and F. Larios, Phys. Rev. D **87**, 074015 (2013).
- [26] J. Drobnak, S. Fajfer and J. F. Kamenik, Nucl. Phys. B **855**, 82 (2012).
- [27] C. Bernardo *et al*, Phys. Rev. D **90** (2014) 113007.
- [28] S. Chatrchyan *et al.* [CMS Collaboration], JHEP **1310**, 167 (2013).
- [29] S. Chatrchyan *et al.* [CMS Collaboration], JHEP **1212**, 035 (2012).
- [30] V. Khachatryan *et al.* [CMS Collaboration], JHEP **1406**, 090 (2014).
- [31] A. Jafari [CMS and ATLAS Collaborations], arXiv:1411.7521 [hep-ex].
- [32] C. -R. Chen, F. Larios and C. -P. Yuan, Phys. Lett. B **631**, 126 (2005); J. A. Aguilar-Saavedra, N. F. Castro and A. Onofre, Phys. Rev. D **83**, 117301 (2011);
- [33] J. A. Aguilar-Saavedra and J. Bernabeu, Nucl. Phys. B **840**, 349 (2010).
- [34] M. Fabbrichesi, M. Pinamonti and A. Tonero, Eur. Phys. J. C **74** (2014) 3193 [arXiv:1406.5393 [hep-ph]].
- [35] C. Degrande, J. Phys. Conf. Ser. **452**, 012009 (2013) [arXiv:1302.1101 [hep-ph]].
- [36] CMS Collaboration, CMS-PAS-TOP-13-008.
- [37] J. A. Aguilar-Saavedra and S. A. dos Santos, Phys. Rev. D **89**, 114009 (2014); B. Tweedie, Phys. Rev. D **90** (2014) 094010.
- [38] T. A. Aaltonen *et al.* [CDF Collaboration], Phys. Rev. Lett. **113** (2014) 261804.
- [39] N. Kidonakis, Phys. Rev. D **74**, 114012 (2006).
- [40] N. Kidonakis, arXiv:1311.0283 [hep-ph]. See also, Phys. Rev. D **83**, 091503 (2011).
- [41] A. Czarnecki, J. G. Korner and J. H. Piclum, Phys. Rev. D **81**, 111503 (2010).
- [42] A. Belyaev, N. D. Christensen and A. Pukhov, Comput. Phys. Commun. **184**, 1729 (2013) [arXiv:1207.6082 [hep-ph]].
- [43] Atlas Coll., Phys. Lett. B **740** (2015) 118 [arXiv:1410.0647 [hep-ex]].
- [44] J. Alwall, M. Herquet, F. Maltoni, O. Mattelaer, T. Stelzer, J. High Energy Phys. **06** (2011) 128.
- [45] J. Alwall, R. Frederix, S. Frixione, V. Hirschi, F. Maltoni, O. Mattelaer, H.-S. Shao, T. Stelzer, P.

- Torrielli, M. Zaro, J. High Energy Phys. **07** (2014) 079.
- [46] E. Conte, B. Fuks, G. Serret, Comput. Phys. Commun. **184** (2013) 222-256 [arXiv:1206.1599 [hep-ph]].
- [47] D. P. Barber *et al.*, Phys. Lett. **B343** (1995) 436.
- [48] G. Moortgat-Pick *et al.*, Phys. Rept. **460** (2008) 131.
- [49] R. Schwienhorst [ATLAS, CMS, D0 and CDF Collaborations], “*Top cross sections and single top,*” in Proceedings of the 33rd International Symposium on Physics in Collision (PIC 2013), Int. J. Mod. Phys. Conf. Ser. **31** (2014) 1460277 [arXiv:1403.0513 [hep-ex]].
- [50] CMS Coll., JHEP **11** (2012) 067 [arXiv:1208.2671]; CMS Coll., JHEP **02** (2014) 024 [arXiv:1312.7582]; ATLAS Coll., Eur. Phys. J. C **74** (2014) 3109 [arXiv:1406.5375]; ATLAS Coll., Phys. Rev. D **91** (2015) 052005 [arXiv:1407.0573]; J. Brochero [CMS and ATLAS Collaborations], arXiv:1412.7176 [hep-ex].
- [51] S. Moretti and K. Odagiri, Phys. Rev. D **57**, 3040 (1998).
- [52] CMS Coll., Phys. Lett. B **720** (2013) 83 [arXiv:1212.6682].
- [53] ATLAS Coll., Phys. Lett. B **711** (2012) 244 [arXiv:1201.1889]; J. Morris [ATLAS Collaboration], “*Top quark pair production cross section at LHC in ATLAS,*” in the Proceedings of the Second Annual Conference on Large Hadron Collider Physics, Columbia Univ., New York, June 2014, arXiv:1409.3382 [hep-ex].
- [54] R. Schwienhorst, C.-P. Yuan, C. Mueller, Q.-H. Cao, Phys. Rev. D **83** (2011) 034019.
- [55] A. Alloul, N. D. Christensen, C. Degrande, C. Duhr, B. Fuks, Comput. Phys. Commun. **185**, 2250 (2014).
- [56] J. Shelton, Phys. Rev. D **79**, 014032 (2009)
- [57] E. L. Berger, Q. H. Cao, J. H. Yu and H. Zhang, Phys. Rev. Lett. **109**, 152004 (2012); E. L. Berger, Q. H. Cao, C. R. Chen and H. Zhang, Phys. Rev. D **83**, 114026 (2011); J. A. Aguilar-Saavedra and S. A. dos Santos, Phys. Rev. D **89**, 114009 (2014); Q.-H. Cao, R. Schwienhorst, J. A. Benitez, R. Brock, C.-P. Yuan, Phys. Rev. D **72** (2005) 094027.

### Appendix A: Cross section parameterization

In this appendix we gather, for reference, the numerical values of the coefficients in Eqs. (8), (9) and (17). See Tables XIX–XXII.

### Appendix B: Stability of parton-level bounds

We have focused in the main body of this paper on obtaining bounds on the anomalous couplings appearing in the effective Lagrangians (1) and (3). We considered a certain observable  $X$  such as the cross section  $\sigma$  or an asymmetry associated with a kinematical variable and, by assuming that an experimental measurement of  $X$  was consistent with the SM result within the experimental

	$a_{12}$	$a_2$	$a_3$	$a_4$	$a_{15}$	$a_5$
Tevatron	-1.90	3.85	0.89	3.39	-0.12	0.09
LHC7	-0.38	1.68	0.95	1.45	0.141	0.017
LHC8	-0.36	1.73	0.95	1.51	0.143	0.019
LHC14	-0.31	1.84	0.97	1.67	0.148	0.027

TABLE XIX: Coefficients of Eq. (8).

	$b_{12}$	$b_2$	$b_3$	$b_4$	$b_{34}$	$b_{15}$	$b_5$	$b_6$	$b_7$	$b_8$
60 GeV	-0.33	0.86	1.34	2.43	-1.12	-0.12	0.006	0.002	0.006	0.002
140 GeV	-0.31	1.09	1.29	2.45	-0.96	-0.13	0.008	0.002	0.007	0.003
300 GeV	-0.29	1.29	1.26	2.50	-0.84	-0.14	0.01	0.003	0.009	0.003

TABLE XX: Coefficients of Eq. (9).

error  $\Delta\sigma_{\text{exp}}$ , we obtained bounds  $\lambda_{\text{min}} < 0 < \lambda_{\text{max}}$  on an anomalous coupling  $\lambda$  at the level of one standard deviation. As remarked in the previous sections, the bounds obtained from the cross section have a very mild dependence on  $E_e$ . For other observables, such as the various asymmetries considered above, that dependence may be more complex and it may be desirable to characterize it. For that purpose, we introduce a simple measure of the sensitivity of an observable  $X$  to an anomalous coupling  $\lambda$  by

$$\mathcal{S}(X, \lambda) = \frac{1}{\lambda_{\text{max}} - \lambda_{\text{min}}}. \quad (\text{B1})$$

In Figure 16 we show the sensitivity of the hadronic-channel cross section (gray lines in the figure) to  $C_2^r$  and  $g_R^r$  as a function of  $E_e$ . We computed the bounds assuming an experimental error  $\varepsilon_{\text{exp}} = 7\%$ , with the cuts  $H_4$  defined in (14) (solid gray squares in the figure), and also with a modified set of cuts obtained from  $H_4$  by substituting the requirement  $|\eta(j)| < 2.5$  in (14) by the less restrictive one  $|\eta(j)| < 5$  (solid gray circles in the figure). As seen in the figure both sets of cuts lead to essentially the same sensitivity of the cross section to both couplings, especially at  $E_e > 50$  GeV. In all cases the sensitivity of the cross section shows little variation with the energy  $E_e$ . Also shown in Figure 16 is the sensitivity of  $A(\Delta\eta(\bar{b}, j_1))$  to  $C_2^r$  and  $g_R^r$  (black lines in the figure), which is seen to be larger than that of  $\sigma$  over the entire range of  $E_e$ , as is also apparent from tables XIV and XIV. Whereas the dependence on  $E_e$  of the sensitivity of this asymmetry is seen to be essentially flat when computed with the cuts  $H_4$  with  $|\eta(j)| < 2.5$  (solid black squares in the figure), it has a sharp peak about  $E_e = 50$  GeV when that cut is relaxed to  $|\eta(j)| < 5$  (solid



$\mathcal{P}_e = 0.0$				$\mathcal{P}_e = 0.0$				$\mathcal{P}_e = 0.4$			
$E_e[\text{GeV}]$	60	140	300	$E_e[\text{GeV}]$	60	140	300	$E_e[\text{GeV}]$	60	140	300
$b_2$	1.23	1.56	1.82	$d_2$	2.43	2.65	2.86	$b_6 \times 10^2$	0.425	0.537	0.701
$b_3$	2.52	2.38	2.34	$d_3$	2.52	2.38	2.37	$b_7 \times 10^2$	1.18	1.62	2.15
$b_4$	4.31	4.28	4.30	$d_4$	4.33	4.30	4.30	$b_8 \times 10^2$	0.471	0.586	0.753
$b_5$	0.0062	0.0086	0.0119	$b_{12}$	-1.37	-1.32	-1.32	$\mathcal{P}_e = 0.7$			
$b_6$	0.0018	0.0023	0.0030	$b_{13}$	-0.061	-0.065	-0.072	$b_6 \times 10^2$	1.03	1.31	1.71
$b_7$	0.0051	0.0069	0.0092	$b_{14}$	0.107	0.103	0.104	$b_7 \times 10^2$	2.86	3.93	5.22
$b_8$	0.0020	0.0025	0.0033	$b_{15}$	-0.123	-0.134	-0.145	$b_8 \times 10^2$	1.14	1.43	1.83

TABLE XXI: Coefficients in Eq. (17) for unpolarized and polarized cross section in leptonic channel. The values of  $d_{6,7,8}$  are the same as those of  $b_{6,7,8}$  shown in this Table.

$\mathcal{P}_e = 0.0$				$\mathcal{P}_e = 0.0$				$\mathcal{P}_e = 0.4$			
$E_e[\text{GeV}]$	60	140	300	$E_e[\text{GeV}]$	60	140	300	$E_e[\text{GeV}]$	60	140	300
$b_2$	1.45	1.87	2.19	$d_2$	2.64	2.89	3.12	$b_6 \times 10^2$	0.581	0.640	0.765
$b_3$	2.61	2.46	2.44	$d_3$	2.60	2.47	2.41	$b_7 \times 10^2$	1.501	1.847	2.323
$b_4$	4.93	4.56	4.43	$d_4$	4.95	4.56	4.46	$b_8 \times 10^2$	0.617	0.683	0.822
$b_5$	0.0076	0.010	0.013	$b_{12}$	-1.22	-1.30	-1.35	$\mathcal{P}_e = 0.7$			
$b_6$	0.0025	0.0027	0.0033	$b_{13}$	-0.074	-0.074	-0.069	$b_6 \times 10^2$	1.408	1.551	1.850
$b_7$	0.0065	0.0079	0.010	$b_{14}$	0.111	0.105	0.096	$b_7 \times 10^2$	3.649	4.490	5.635
$b_8$	0.0027	0.0029	0.0035	$b_{15}$	-0.142	-0.150	-0.158	$b_8 \times 10^2$	1.500	1.664	1.998

TABLE XXII: Coefficients in Eq. (17) for unpolarized and polarized cross section in hadronic channel. The values of  $d_{6,7,8}$  are the same as those of  $b_{6,7,8}$  shown in this Table.

black circles). The peak is especially pronounced in the sensitivity to  $g_R^r$ .

It is not obvious that a sensitivity profile with such rapid variations with  $E_e$  would not be drastically altered by the incorporation of radiative corrections, showering and hadronization in the computation of the asymmetry. Since those more detailed computations are beyond the scope of the present preliminary study, we have not considered in this paper observables whose sensitivity has a strong dependence with  $E_e$ . In the particular case of  $A(\Delta\eta(\bar{b}, j_1))$ , the very tight bounds obtained at  $E_e = 60$  GeV on  $g_R^r$  and other effective couplings when the cut  $|\eta(j)| < 5$  is used are probably an artifact of the tree-level partonic approximation used here, and therefore potentially misleading. It is for this reason that we chose the more restrictive cut on  $|\eta(j)| < 2.5$  in (14), with which we obtain bounds that are somewhat less tight at low energies but also more reliable.

In Figure 17 (a) we show the sensitivity of the asymmetry  $A(\Delta y(\bar{t}, j_1))$  to the anomalous

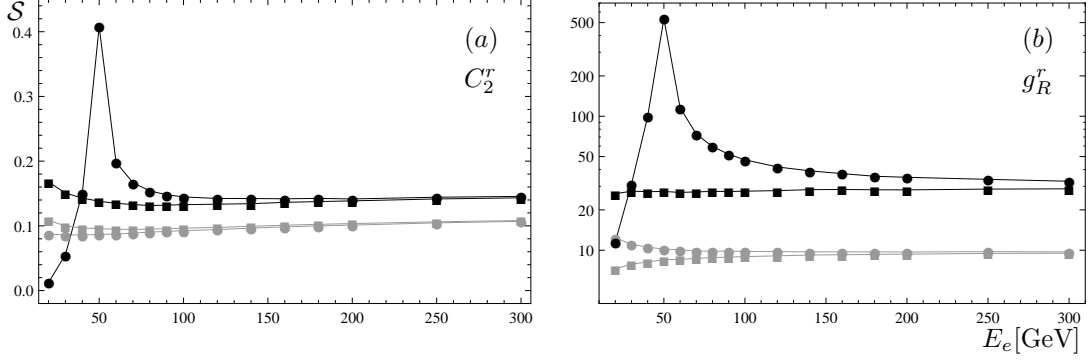


FIG. 16: Sensitivity  $\mathcal{S}$  of the cross section (gray markers) and the asymmetry  $A(\Delta\eta(\bar{b}, j_1))$  (black markers) to the effective couplings (a)  $C_2^r$  and (b)  $g_R^r$ , computed with the cuts  $H_4$  defined in (14) with  $|\eta(j_1)| < 2.5$  (solid boxes) and  $|\eta(j_1)| < 5$  (solid circles). The experimental error is assumed to be  $\varepsilon_{\text{exp}} = 7\%$ . The lines are only to guide the eye.

couplings  $V_R^r$ ,  $g_R^r$ ,  $g_R^i$ ,  $g_L^r$ ,  $C_2^r$  as a function of  $E_e$ . As already remarked in section V B, the sensitivity of this asymmetry at  $E_e = 60$  GeV is much larger than at 140 and 300 GeV. The figure shows that the sensitivity has a peak at about  $E_e = 40$  GeV where it is larger than the average sensitivity at higher energies by a factor 3–10 depending on the coupling. Thus, the bounds obtained from this asymmetry at  $E_e = 60$  GeV are enhanced by the proximity of the peak and therefore possibly unreliable. For energies  $E_e \geq 120$  GeV the dependence of the sensitivity on  $E_e$  is much weaker, as seen in the figure, which suggests to us that the bounds in that region are more realistic than at lower energies.

Figure 17 (b) shows the sensitivity of the asymmetry  $A(\cos(\bar{t}_{\text{c.m.}}, j_{1*}))$  (black markers) to the anomalous couplings  $V_R^r$  (solid squares), and  $C_3^r$  (solid circles) as a function of  $E_e$ . Also shown for reference is the sensitivity of the cross section (gray markers). As is already apparent from Table XVIII, and can be seen in more detail in the figure, the sensitivity of this asymmetry increases monotonically with  $E_e$  (by a factor  $\gtrsim 2$  as  $E_e$  varies from 30 to 300 GeV) without peaks or rapid oscillations.

A class of asymmetries not discussed in section V B is based on longitudinal-boost non-invariant kinematic observables in lab frame involving longitudinal neutrino momenta. Among those, we have considered  $\cos(\bar{t}, \nu_e)$ ,  $\cos(j_{1,2}, \nu_e)$ ,  $\cos(\bar{b}, \nu_e)$ ,  $\cos(W, \nu_e)$ . These observables yield tight bounds on  $C_{2,3,4}^{r,i}$  at  $E_e = 60$  GeV. Their sensitivity, however, seems to vary rapidly with  $E_e$ , becoming very small at  $E_e = 140$  GeV but large at the other two energies. For instance, for  $C_2^r$  from the asymmetry of  $\cos(j_2, \nu_e)$  we find the bounds  $\pm 2.87$ ,  $\pm 5.54$ ,  $\pm 0.91$  at  $E_e = 60$ , 140 and 300 GeV, respectively, with an assumed experimental error of  $\varepsilon_{\text{exp}} = 7\%$ . For  $C_3^r$  from the asymmetry of

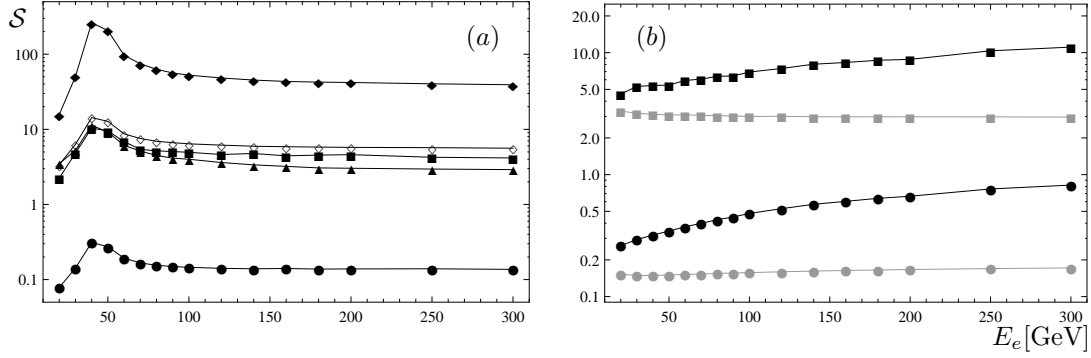


FIG. 17: (a) Sensitivity of the asymmetry  $A(\Delta y(\bar{t}, j_1))$  to  $C_2^r$  (solid circles),  $V_R^r$  (solid squares),  $g_L^r$  (solid triangles),  $g_R^r$  (solid diamonds) and  $g_R^i$  (open diamonds). (b) Sensitivity of the asymmetry  $A(\cos(\bar{t}_{c.m.}, j_{1*}))$  (black markers) and of the cross section (gray markers) to  $C_3^r$  (solid circles) and  $V_R^r$  (solid squares). All observables computed with the cuts  $H_4$  defined in (14). The experimental error is assumed to be  $\varepsilon_{\text{exp}} = 7\%$ . The lines are only to guide the eye.

$\cos(\bar{t}, \nu_e)$  we find the bounds  $\pm 2.15$ ,  $\pm 7.67$ ,  $\pm 1.87$ , and for  $C_4^r$  from the asymmetry of  $\cos(\bar{b}, \nu_e)$  we get  $\pm 3.11$ ,  $\pm 6.0$ ,  $\pm 5.16$ , at the same energies and with the same experimental error. It is because of that suppressed sensitivity at the intermediate energy that bounds from these observables are not discussed in section VB.